

JGR Solid Earth

RESEARCH ARTICLE

10.1029/2019JB018395

Key Points:

- In this study, we extended the Wave Gradiometry method of a plane wavefield to estimate the azimuthal anisotropy
- The fast orientations of anisotropy extracted by Wave Gradiometry are generally consistent with the large fault system and orogenic belt in the southeastern Tibetan Plateau
- The azimuthal anisotropies of Rayleigh wave extracted by Wave Gradiometry provide further constraints on the uncertainty of S wave splitting

Supporting Information:

- Supporting Information S1
- Table S1
- Table S2
- Table S3
- Table S4
- Table S5
- Table S6
- Table S7
- Table S8
- Table S9
- Table S10
- Table S11

Correspondence to:

C. Liang,
liangct@cdut.edu.cn

Citation:

Cao, F., Liang, C., Zhou, L., & Zhu, J. (2020). Seismic azimuthal anisotropy for the southeastern Tibetan Plateau extracted by Wave Gradiometry analysis. *Journal of Geophysical Research: Solid Earth*, 124, e2019JB018395. <https://doi.org/10.1029/2019JB018395>

Received 17 JUL 2019

Accepted 15 APR 2020

Accepted article online 20 APR 2020

Seismic Azimuthal Anisotropy for the Southeastern Tibetan Plateau Extracted by Wave Gradiometry Analysis

Feihuang Cao^{1,2} , Chuntao Liang^{1,2} , Lu Zhou², and Jieshou Zhu²

¹State Key Laboratory of Geohazard Prevention and Geoenvironment Protection, Chengdu University of Technology, Chengdu, China, ²Key Laboratory of Earth Exploration and Information Techniques of the China Ministry of Education, Chengdu, China

Abstract Wave Gradiometry (WG) is a dense array data processing method used to extract seismic velocity and other properties of the earth. In this study, we propose using WG for a plane wave field to measure azimuthal anisotropy by fitting the phase velocities from different back azimuths. We applied this new method to the Temporary Western Sichuan Array and obtained the isotropic and azimuthal anisotropy for period bands centered at $T = 20, 40$, and 60 s in the southeast Tibetan Plateau. Our results show that the fast orientations of anisotropy are well consistent with the strikes of the fault system and orogenic belt. The weak anisotropic magnitude in the northern part of the south Chuandian subblock and a consistency of fast orientation in boundary fault zone (BFZ) at different periods may be attributed to anisotropic relics associated with the Emeishan Large Igneous Province. Comparing our results with those of previous studies, we found that our anisotropic results are consistent with anisotropic structures measured by the Pms phase in the plateau area, while a systematical angular difference exists in the BFZ, Sichuan Basin, and south Chuandian subblock where high Rayleigh wave phase velocity was observed. The Lijiang-Xiaojin fault and Longmenshan fault appear to form a deep-rooted strong boundary at the lithospheric scale, as they serve as a boundary for anisotropic structures, isotropic velocity, and the other three WG parameters.

1. Introduction

In 2006, Langston used the finite difference method to extract waveform gradient parameters of the small-scale linear array for studying the strong ground motion of the Mississippi Bay. In 2007, the 2-D Wave Gradiometry (WG) method for the time and frequency domains was theoretically proposed (Langston, 2007a, 2007b, 2007c; Langston et al., 2006). Based on these studies, Sollberger et al. (2016) developed the lunar velocity model. Furthermore, Poppeliers (2010, 2011) used the wavelet transform method to extract wave gradients. Poppeliers et al. (2013) and Poppeliers and Punosevac (2013) proposed the 3-D WG method. To adapt to irregular large-scale dense arrays, Liang and Langston (2009) proposed a weighted inversion method for computing the spatial gradient together with the reducing velocity method. WG poses a few advantages of the inversion of the deep earth structure: It requires only one earthquake to find a relatively stable Rayleigh wave phase velocity structure for a period of $T \geq 20$ s. Zhou et al. (2017) converted original waveforms to different components according to the azimuth computed by WG and then obtained the WG parameters of three components for the central and eastern United States. They discussed the radial anisotropy based on the Love and Rayleigh wave velocity based on the WG analysis. In addition, the WG method has been applied for wavefield reconstruction (Maeda et al., 2016), and the vertical WG method has been used to extract impedance and attenuation structures in the vicinity of boreholes (Langston & Ayele, 2016). Furthermore, Porter et al. (2016) combined ambient noise tomography with WG to calculate a three-dimensional S wave velocity structure.

Lin et al. (2009, 2011) and Jin and Gaherty (2015) applied a Helmholtz tomography method to obtain local phase velocity and anisotropy from a dense array. This method is based on the Helmholtz equation and yields estimation of structural phase velocity. However, it does not analyze the geometrical spreading and radiation patterns in depth as the WG does, and it focuses more on the second derivatives. Liu and Holt (2015) link the WG parameters of A and B coefficients to the Helmholtz solutions, and they assumed that the spatial gradients and WG parameters within a subarray define a spatially variable and continuous

field. Edme and Yuan (2016) used spatial gradients to estimate a local dispersion curve from seismic ambient noise, and they used singular-value decomposition to determine the polarization ratio and ellipticity in time-frequency windows to improve efficiency and robustness.

Seismic azimuthal anisotropy provides key evidence on lithosphere deformation and tectonic movement. In terms of the causes of anisotropy, vertical basalt walls in the lithosphere, the orientation arrangement of liquid-filled microfractures, the alignment of plates in collision zones, inverted sedimentary layers and lattice-preferred orientations, and so forth can result in horizontal symmetry axis anisotropy, and these factors are related to tectonic movement, stress fields, and tectonic deformation (Babuska & Cara, 1991; Boness, 2004; Crampin et al., 1991; Sayers, 1994; Stein & Wysession, 2003). Hess (1964) used Pn waves to study the anisotropy of the upper mantle of the Pacific Ocean, serving as a prelude to modern seismological anisotropy research; Crampin (1966) discovered the anisotropy of the upper mantle based on the high-order surface wave in Eurasia; Crampin et al. (1980) were the first to confirm the presence of S wave splitting in the crust in Turkey.

De Ridder and Curtis (2017) deduced a second-order anisotropic elliptic equation of high-frequency noise surface wave energy based on information on wave gradients and then estimated the azimuthal anisotropy of the shallow surface of the Ekofisk. The second-order spatial gradient can generally reduce truncation errors, but it works best for a rectangular array. In recent years, azimuthal anisotropies have been extracted for the eastern Tibetan Plateau using surface waves (Ceylan et al., 2012; Legendre et al., 2015; Su et al., 2008; Sun et al., 2015; Xie et al., 2013, 2017), Pms phases (Sun et al., 2012; Sun et al., 2015; Zheng et al., 2018), and Pn waves (Liang et al., 2004).

The radial anisotropy estimated by shear wave splitting has a relatively high and reliable lateral resolution. SKS and ScS splitting times correspond to the average anisotropy of the mantle to the surface, but it is generally believed that XKS splitting mainly occurred in the upper mantle (Chang et al., 2015; Sol et al., 2007; Soto et al., 2012; Wang et al., 2008; Yang et al., 2018); Pms splitting is influenced by the entire crust (Chen et al., 2013; Kong et al., 2016; Legendre et al., 2015; Sun et al., 2012; Sun et al., 2015; Zheng et al., 2018). However, the poor radial resolution of the anisotropy of shear wave splitting places some limitations on the interpretation of lithospheric deformation and tectonic movement.

The southeast Tibetan Plateau is one of the most seismically active areas in China. This region is located at the junction of three major active blocks: the Songpan-Garze Block, Chuandian block, and South China Block (Figure 1a). In addition, forming the southeast margin of the Tibetan Plateau, this area shows signs of complex tectonic deformation due to the influence of the northward subduction of the Indian plate and the eastward subduction of the Burmese microplate along the Burma arc (Li et al., 2008; Ni et al., 1989). In the late Cretaceous, the Tethys Sea gradually started to close, causing the Indian plate to drift northward and collide with the Eurasian Plate in the Eocene. Blocked by the Tarim Basin and North China Block, crust in the Tibetan Plateau was shortened and thickened. The accumulated materials then escaped eastward and southeastward, resulting in complex and active geological tectonics in the Tibetan Plateau and its marginal areas (Searle et al., 1987). This process resulted in a series of strong seismic patterns (Deng et al., 2003). Over the past 20 years, roughly 200 moderate and severe earthquakes ($\geq M5$) occurred in this area (collecting from <https://earthquake.usgs.gov>), including the catastrophic Wenchuan, Lushan, and Jiuzhaigou earthquakes of the last 11 years. Current tectonic movement is still active (Cheng et al., 2012; Liang et al., 2018; Liu et al., 2018; Matsushita et al., 2019; Wang et al., 2018; Zhou, 2008), and future seismic risk is still very high. Therefore, understanding tectonic processes and deep geodynamics in the southeastern margins of the Tibetan Plateau is very important for scientific research, earthquake prevention, and hazard mitigation. To understand this seismic activity more deeply, deformation mechanisms of the lithosphere are a key point.

Moreover, deformation mechanisms of the lithosphere in the southeast margins of the eastern Tibetan Plateau remain controversial. The three mainstream views of these processes are represented by the middle-lower crust flow model, the pure shearing model, and the model of the viscous flow of the whole lithosphere (Bai et al., 2010; Burchfiel et al., 1995; Houseman & England, 1993; Klemperer, 2006; Liu et al., 2014; Molnar et al., 1993; Royden et al., 1997; Yang et al., 2018; Zhu et al., 2017). The pure shearing model argues that the brittle deformation of the upper crust is the dominant mechanism accounting for uplift (Hubbard et al., 2010; Hubbard & Shaw, 2009; Tapponnier et al., 1982) while the middle-lower crust flow model argues that interlayer slippage decoupling and the blockage of the Sichuan Basin caused the

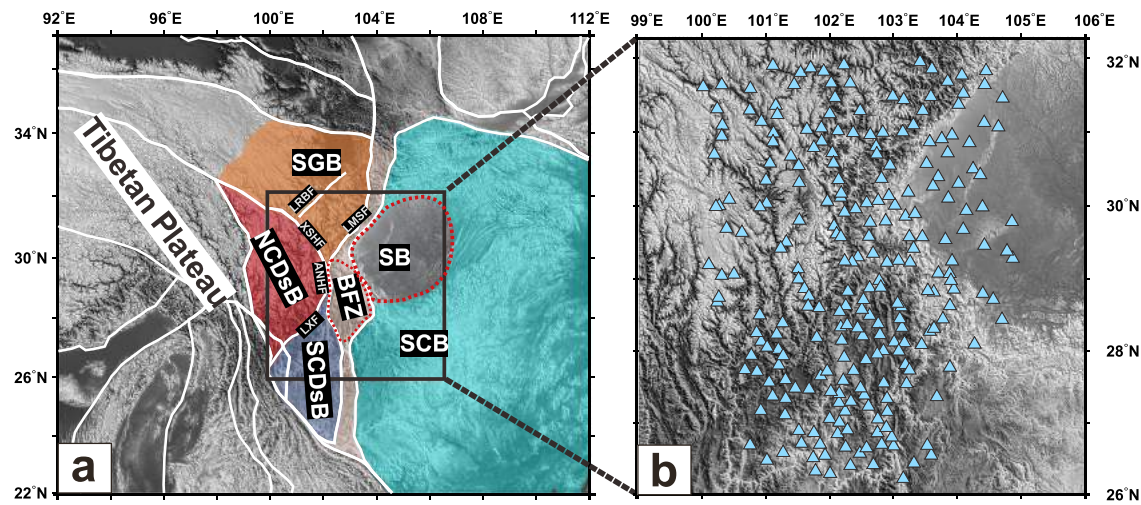


Figure 1. Geological setting (a) and seismic array used in this study (b). In (a): white lines denote the boundaries of tectonic blocks. SGB = Songpan-Ganzi block; SCB = South China Block; SCDSB = south Chuandian subblock; NCDSB = north Chuandian subblock; ANHF = Anning He Fault; LMSF = Longmenshan fault; XSHF = Xianshuihe fault; BFZ = boundary fault zone; LXF = Lijiang-Xiaojin fault. In (b): light blue triangles denote stations of the Temporary West Sichuan Array (TWSA).

lower crust flow, resulting in vertical expansion and uplift (Burchfiel et al., 1995; Klempner, 2006; Royden et al., 1997). The model of the viscous flow of the whole lithosphere suggests that the convective removal of the lower lithosphere beneath the Tibetan Plateau can account for a rapid increase in the mean elevation of the Tibetan Plateau (Molnar et al., 1993). In addition, Yao et al. (2008, 2010) and Liu et al. (2014) suggest that the complex deformation mechanisms of the southeast margin of the Tibetan Plateau cannot simply be fitted in a unified model. Yao et al. (2010) suggest that long-distance uninterrupted crustal flow is difficult to coordinate with the low-velocity zone determined by receiver functions (Wang et al., 2010) and surface wave imaging (Yao et al., 2008). In addition, evidence of coexisting channel flow and pure-shear crustal thickening in the Tibetan Plateau has been deduced by complex azimuthal anisotropy (Agius & Lebedev, 2017) and the 3-D S wave velocity structure (Liu et al., 2014). Radial anisotropic studies (Xie et al., 2017) suggest that brittle deformation transmitted to ductile deformation from the upper crust to the deeper crust in the interior Tibetan Plateau while middle-lower crust flows rotated near the borders of Tibet. Moreover, the influence of gravitation on lithosphere deformation and the migration of Tibetan material has also been taken into account in some cases (Huang et al., 2018; Li et al., 2017). Of course, due to the earth's complexities, a unified conclusion still cannot be made. In this study, we use the WG method detailed by Liang and Langston (2009) to estimate phase velocities from different back azimuths, and these are fitted to find the two azimuthal anisotropy parameters and isotropic velocity. This is the new study to extract azimuthal anisotropies based on the WG method with the plane wave assumption. The reducing velocity and weighted inversion methods are used to mitigate the bias caused by the irregular station distribution. By synthetic data testing, we demonstrate that the WG is reliable in estimating the anisotropy for periods of longer than 20 s. The azimuthal anisotropy extracted by the WG method may provide some constraints for consideration in other anisotropic research.

2. Data

From October 2006 to July 2009, the Temporary Western Sichuan Array (TWSA) with more than 230 CMG-3ESPC (60 s–50 Hz) wide-band seismographs was deployed in the southeastern Tibetan Plateau by the Institute of Geophysics, China Earthquake Administration (Figure 1b). Seismic data of the TWSA have been used extensively in many studies (ChinArray, 2006) (e.g., to compute focal mechanism solutions to evaluate the shock-location error of the May 12 Wenchuan earthquake, Liu et al., 2009; in the joint inversion of receiver functions and surface wave dispersion to image the high-resolution structure of the eastern margin of Tibet, Liu et al., 2014; Yu et al., 2010; in using ray tracing to discuss the influence of ray path to surface wave tomography, Li et al., 2015; in using P wave tomography to study the uplift of Longmenshan, Guo

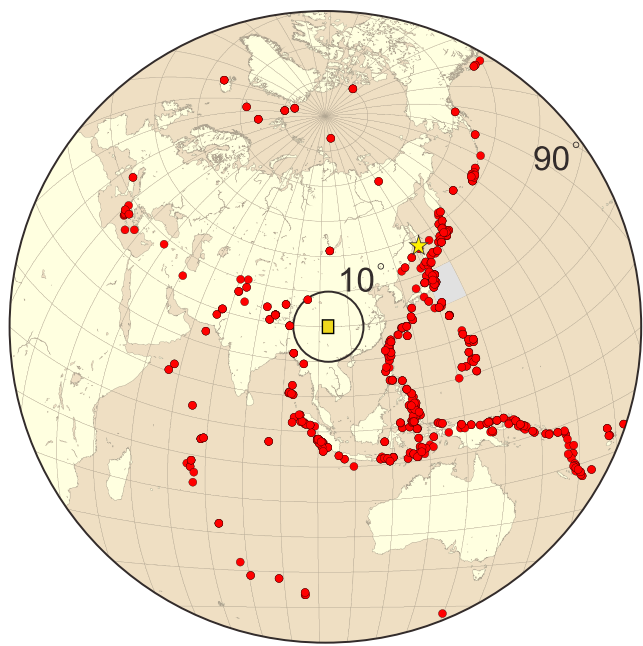


Figure 2. Epicenters of events used in this study. Red dots represent the earthquakes used in this study. Yellow box in the central present the study area, the yellow pentacle is the epicenter of Tatar Strait earthquake (Russia). Two black circles denote the distances to the center of the study area.

ness p with by $p' = p - \bar{p}$ (Langston, 2007b; Liang & Langston, 2009). Four parameters (seismic velocity v , wave azimuth θ , radiation pattern A_θ , and geometrical spreading A_r) can be extracted from the spatial gradients of a waveform by WG (Langston, 2007a, 2007b, 2007c; Langston et al., 2006; Liang & Langston, 2009; Zhou et al., 2017). Supporting information given in Figure S1 shows the geometry of a subarray and the corresponding waveforms. Figure S2 shows the WG results for the subarray shown in Figure S1. In our WG analysis of earthquakes from different back azimuths, we found that phase velocities vary significantly with different back azimuths (Figure S3).

Theoretically, the horizontal resolution of WG parameters is related to the width of a subarray and the period band. As the periods ($T = 20, 40$, and 60 s) used in this study are shorter than those used in Liang and Langston (2009) and Zhou et al. (2017) ($T = 120$ s), the radius of a subarray is given as 50 km, and the phase velocities of different periods are averaged on spatial scales of $30, 65$, and 80 km for $T = 20, 40$, and 60 s, respectively, before anisotropic fitting (Figure S4).

Once more earthquakes from different back azimuths were analyzed, we found that phase velocities vary with back azimuths as a second-order cosine function (Figure 3a). In this study, we take one further step in computing the azimuthal anisotropies. Assuming that the percentage of Rayleigh wave azimuthal anisotropy is small in a stratified half-space, the phase velocity shifts systematically as a trigonometric function of 2θ with θ being the back azimuth (Backus, 1965; Smith & Dahlen, 1973)

$$v(f, \theta) = \bar{v}(f) + a(f)\cos(2\theta) + b(f)\sin(2\theta), \quad (1)$$

where f denotes the frequency, θ is the back azimuth, and \bar{v} is the isotropy velocity. Coefficients a and b are dependent on the 21 anisotropic elastic parameters of the material through which the waves are propagating (Backus, 1965). Then forms of magnitude of anisotropic and fast orientation are

$$M = 2\sqrt[2]{a^2 + b^2} \frac{1}{v_0}, \quad (2)$$

$$\varphi = \tan(b/a)/2, \quad (3)$$

et al., 2009; and in adopting the Pms phase of receiver function to estimate the crustal anisotropy, Zheng et al., 2018).

The geological locations (100 – 105° E, 26 – 32° N) of the TWSA are shown in Figure 1, and interstation distances are 10 – 50 km. During installation, the TWSA had recorded more than 1,500 earthquakes ($M \geq 5.5$). Earthquakes deeper than 200 km were omitted from the analysis due to the generally weak surface waves excited. Finally, roughly 165, 304, and 275 events were selected for period bands of 16 – 24 s, 32 – 48 s, and 48 – 72 s, respectively (Figure 2 and supporting information Tables S1–S3). In addition, we disregarded stations with peak amplitudes of approximately 30% larger or smaller than those of surrounding stations to ensure that target Rayleigh phases were clean and strong on all waveforms. Figure 2 shows the locations of the study area and events. Relative good azimuthal coverage is guaranteed by the geometrical distributions of events and the array.

3. Methods

A theoretical background of the WG for a 2-D array was provided by Langston et al. (2006) and Langston (2007c). A method of reducing velocity and weighted inversion for irregular arrays was detailed by Langston (2007b) and Liang and Langston (2009). The reducing velocity method is important because it helps reduce the bias in velocity and anisotropy caused by an irregular array (see section 5.1 for details). Reducing velocity assumes that a medium in a subarray (Figure S1) is homogeneous and that the average phase velocity is known. Thus, we can remove phase shifts due to this average velocity by replacing the slow-

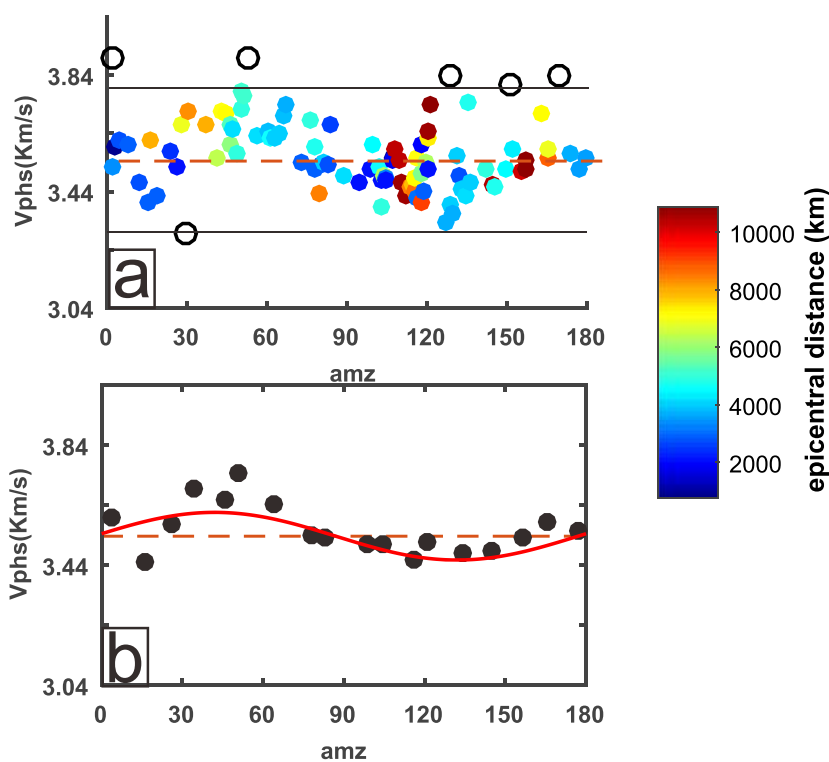


Figure 3. Azimuthal anisotropy measurement for one station. The horizontal axis of (a) and (b) is the back azimuth ranging from 0° to 180° , and the vertical axis is the phase velocity. The color bar denotes the epicentral distance. (a) Colored dots denote the original phase velocity derived by the WG, and the open black circles denote omitted outliers that are 0.25 km/s larger or smaller (limited by two black lines) than the average velocity (brown dashed line). (b) Black dots denote the median value within every 10° azimuth window. These median values are used to fit the anisotropic parameters; the red curved line denotes the fitted curve governed by equation (1).

where M is the anisotropic magnitude, φ is the fast orientation, and v_0 is the isotropic velocity. Once the phase velocity in different periods and different back azimuths are found by WG, equations (1)–(3) can be applied to find the anisotropic parameters and isotropic velocity. To limit the influence of outliers, phase velocities that are 0.25 km/s larger or smaller than the mean velocity of all back azimuths (black circles shown outside of the two black lines in Figure 3a) are excluded in the fitting.

The phase velocity from roughly the same azimuth may not always be equal (solid dots in Figure 3a, the colors of solid dots denote epicentral distances to show that distance did not significantly affect the result) due to wave scattering, wavefront healing, multiple paths, or other local micro earthquakes (the southeastern margin of the Tibetan Plateau is an earthquake-prone area) (Bodin & Maupin, 2008; Friederich et al., 2000; Lin & Ritzwoller, 2011a, 2011b; Tang et al., 2017; Wielandt, 1993). Furthermore, the uneven azimuthal coverage of velocity in this study area constitutes a major challenge to fitting the anisotropic model (equation (1)) from 0° to 360° , and the anisotropic results are not very different when we fitted the anisotropy, from 0° to 360° , with or without the first-order term (see section 5.2.4 for details). So we choose to ignore the first-order term that may be related to backward scattering (Lin & Ritzwoller, 2011a, 2011b). The first-order term shows 360° period azimuthal dependence in the anisotropic fitting. In this study, we subtract azimuths between 180° and 360° by 180° . Second, we divide azimuths into small windows with an interval of 10° and then choose the median velocity of each azimuthal window as a data point to represent the value of the corresponding window (see the black dots in Figure 3b). The median values of all azimuth windows are used to fit equation (1) to find the anisotropic parameters. And Figure 4 shows the anisotropic fitting of stations in different blocks.

Overall, the procedure of applying WG to estimate azimuthal anisotropy is as follows: (1) collect waveform data from the China Earthquake Data Center (CEDC); (2) remove instrument responses, wave trends, and

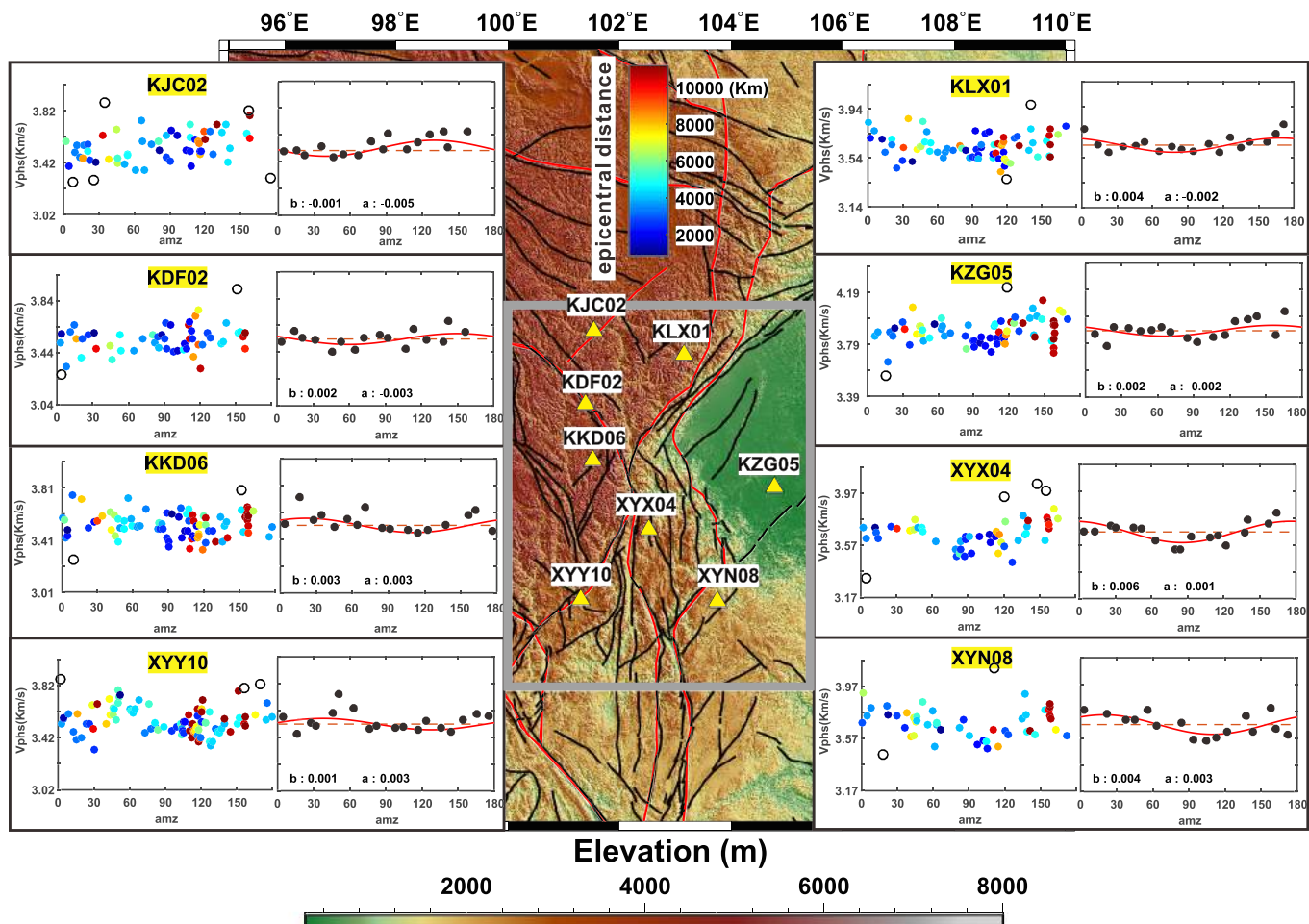


Figure 4. Azimuthal anisotropy measurements for $T = 40$ s in different blocks. Elements included in each subgraph are the same as those included in Figure 3.

means; (3) filter waveform to period bands of 16–24 s, 32–48 s, and 48–72 s with central periods of $T = 20$, 40, and 60 s, respectively; (4) omit stations with peak amplitudes of approximately 30% larger or smaller than those of surrounding stations and ensure the target phases are clean and strong on all waveforms; (5) compute the wave gradient to obtain parameters of v , θ , A_θ , and A_r for each station; (6) calculate the wave gradient parameters of all period bands for all stations in the TWSA; (7) repeat Steps 1 through 6 for earthquakes from different azimuths; and (8) use the median velocity of each azimuthal interval to fit the anisotropy model (equation (1)) using the nonlinear least square method and compute the anisotropic parameters of M and φ . In addition, the bootstrap method is used to measure the standard deviations of magnitudes and fast propagation directions of anisotropies.

4. Results

The process described above is applied to stations of the TWSA. Four WG's parameters and azimuthal anisotropies are obtained for three period bands and are shown in Figures 5 to 8.

4.1. WG Parameter Maps for Different Passbands

Figure 5 shows the four WG parameters for period bands with central periods of $T = 20$, 40, and 60 s, respectively. According to the sensitivity kernel curve shown in Figure S5, the results of $T = 20$, 40, and 60 s are mostly sensitive to the structures at depth ranges of approximately 25, 60, and 90 km, respectively. The isotropic velocity maps of the southeastern Tibetan Plateau are consistent with previous studies by either body wave tomography or surface wave tomography (Fan et al., 2015; He et al., 2017;

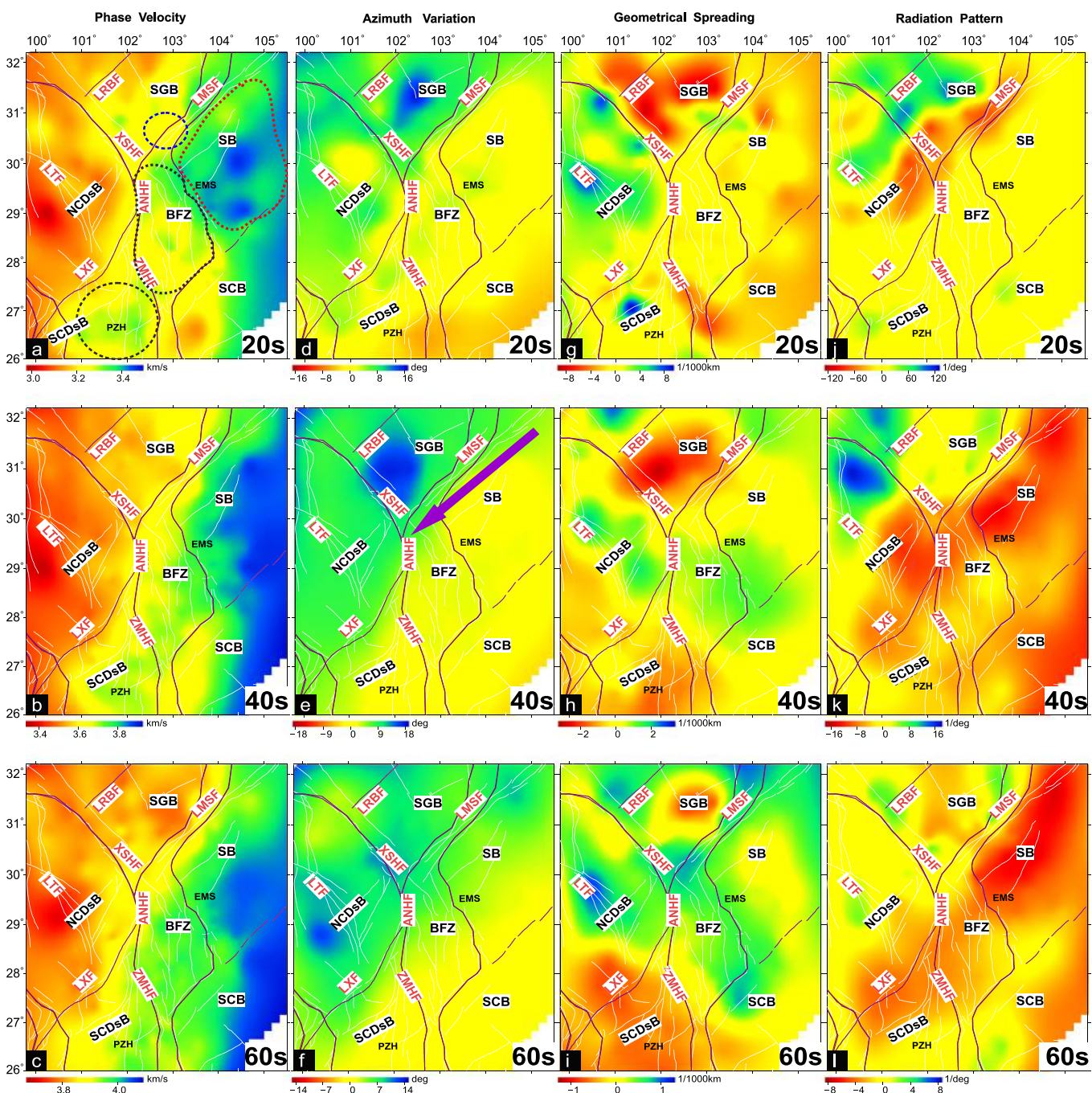


Figure 5. Maps of WG parameters. (a) ~ (c), (d) ~ (f), (g) ~ (i), and (j) ~ (l) denote phase velocity, azimuth variation, geometrical spreading, and radiation patterns for $T = 20, 40$, and 60 s, respectively. The corresponding period is noted in the lower right corner of each subfigure. Purple solid lines denote block boundaries. White solid lines represent faults. LMSF = Longmenshan fault; LRBF = Longriba fault; XSHF = Xianshuihe fault; ANHF = Anninghe fault; LXF = Lingjiang-Xiaojin fault; ZMHF = Zemuhe fault; LTF = Litang fault; SGB = Songpan-Ganzi block; SB = Sichuan Basin; NCDsB = north Chuandian subblock; SCDsB = south Chuandian subblock.

Liu et al., 2018; Liu et al., 2014; Yao et al., 2010), and the other three WG's parameters are connected with velocity boundary and wave direction.

Phase velocities are shown in Figures 5a–5c. Over a large scale, the phase velocities increase from west to east and are largely separated by the block boundaries. For example, the Xiaojin-Lijiang fault separates

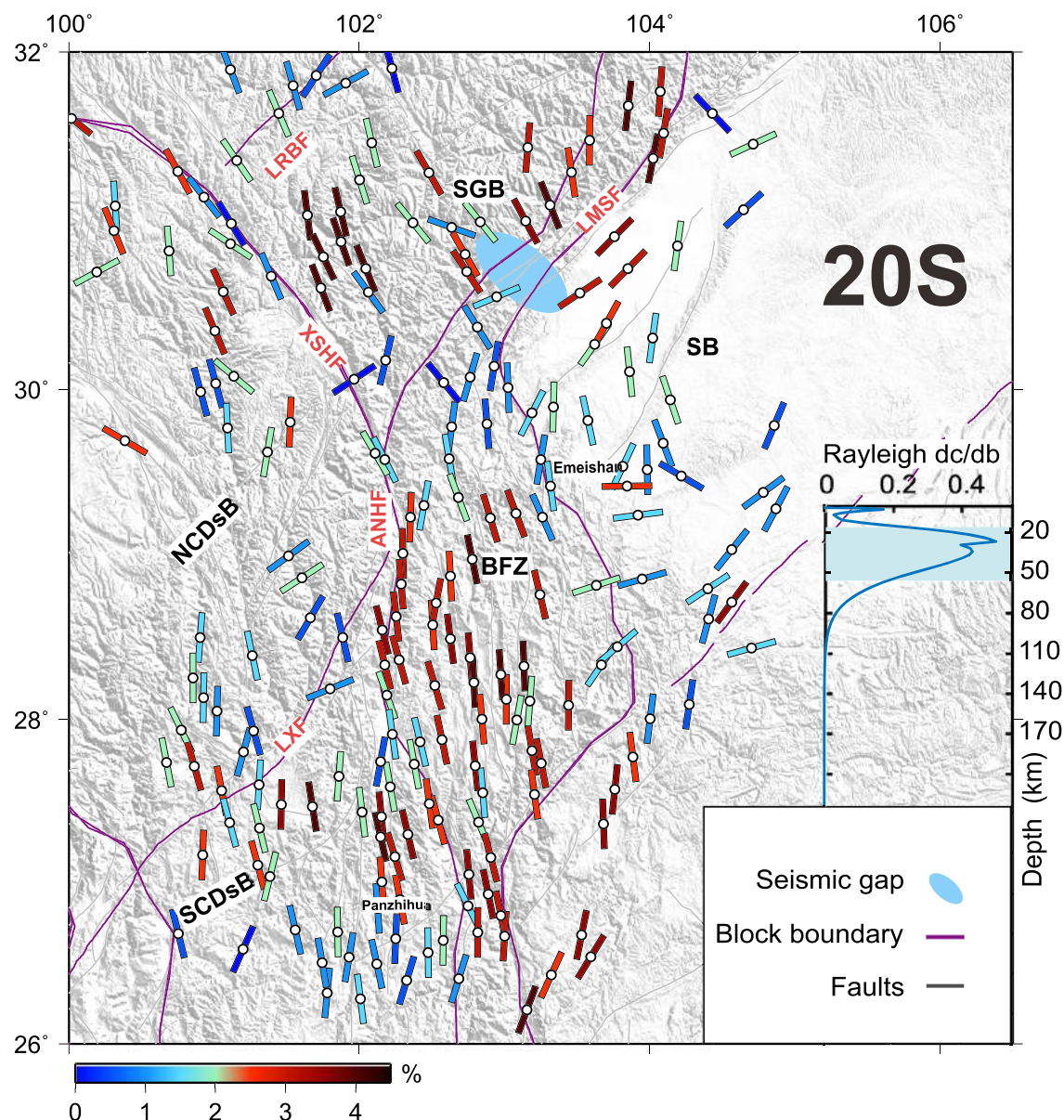


Figure 6. Anisotropic maps of $T = 20$ s. The orientations and colors of bars represent the fast orientation and magnitude of anisotropy, respectively. Gray solid lines denote faults, and purple solid lines denote block boundaries. The light blue oval area denotes the seismic gap in the LMSF, and the blue curve shown in the lower right subfigure denotes the sensitive kernel.

the NCDsB from the SCDsB, and the Longmenshan fault separates the Sichuan Basin from the SGB. The Sichuan Basin, an ancient craton basin (Li et al., 2008), is characterized by high velocities of roughly 3.5, 3.9, and 4.05 km/s for $T = 20$, 40, and 60 s, respectively. In contrast, the north Chuandian subblock and Songpan-Ganzi block are dominated by low velocities. In addition, the SCDsB and boundary fault zone (BFZ) show a relatively high phase velocity, and previous geophysical and geochemistry studies show that igneous rocks are broadly exposed on the surface of the Emeishan Large Igneous Province (ELIP, located in SCDsB and BFZ) which was produced during a massive volcanic eruption in the Middle and Late Permian (Ali et al., 2005, 2010; Chung & Jahn, 1995; Guo et al., 2017; Zhang, 2009; etc.). At smaller scales, the seismic gap in Longmenshan faults has a low-velocity anomaly. That of the north Chuandian subblock is especially low (3.1, 3.5, and 3.8 km/s for $T = 20$, 40, and 60 s, respectively) compared to those of regions spanning the Xianshuihe fault to the northeast and the Lijiang-Xiaojin fault to the east.

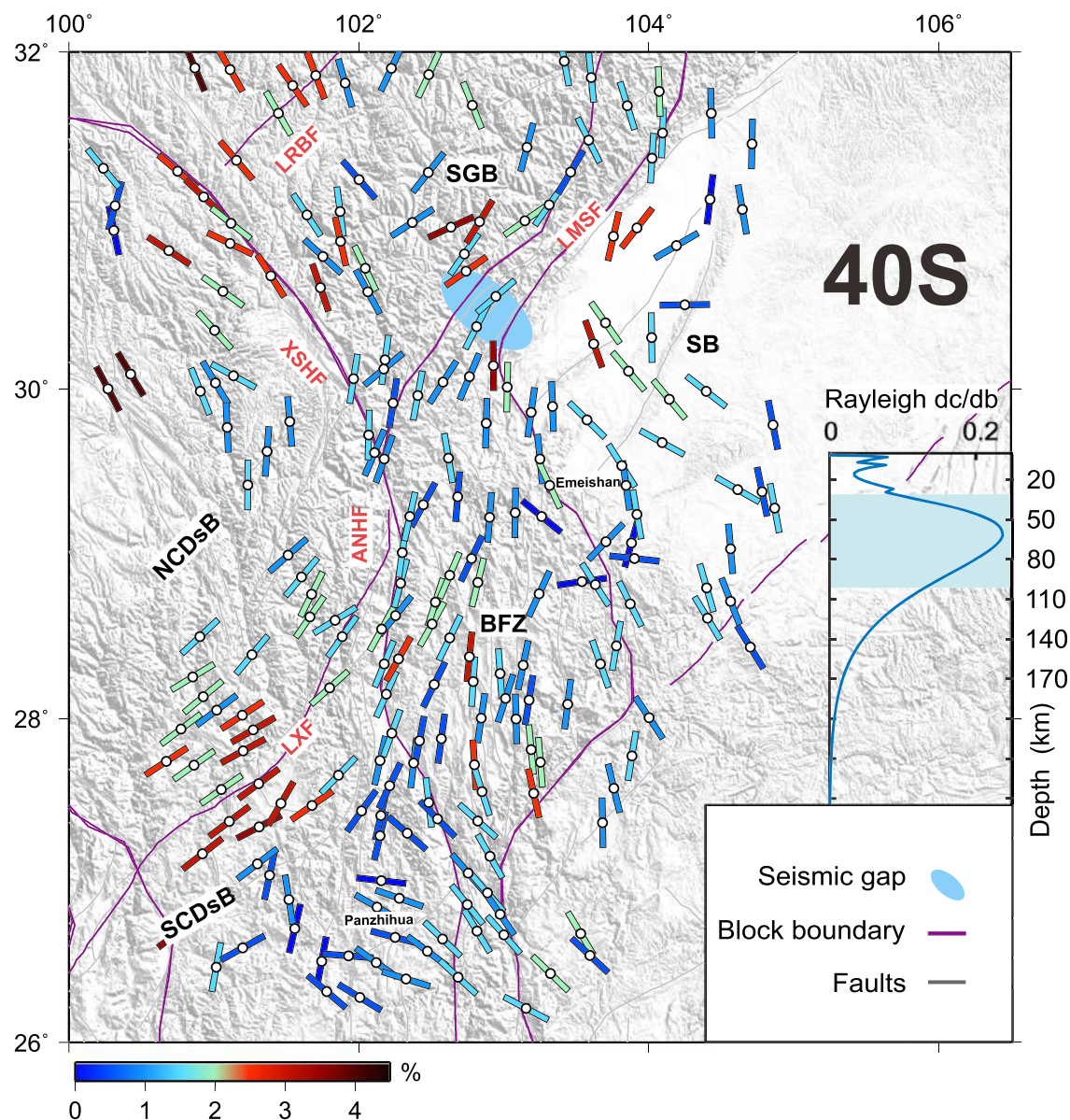


Figure 7. Results given in Figure 7 but for $T = 40$ s.

Figures 5d–5l show maps of the other three WG parameters based on the earthquake occurring in the Tatar Strait, Russia (the yellow pentacle in Figure 2). Figures 5d–5f show azimuth perturbations, which denote the difference between the source-station path and the incident azimuth of surface waves at the corresponding station. The positive azimuth variation denotes that the actual propagation path is offset clockwise relative to the great circle ray path. According to Snell's law, the back azimuth increases when waves are obliquely incident from the high-velocity medium in the east to low-velocity material in the west (supporting information Figure S6). Understandably, a high anomaly of azimuth variation is associated with more complex geological structures. For example, the highest positive azimuth variation is distributed at the Songpan-Ganzi block, and low value azimuth variation appears in stable areas such as the Sichuan Basin and South China Block where azimuth variations are much weaker relative to the plateau area. It is amazing that the Longmenshan and Lijiang-Xiaojin faults serve as a boundary in separating positive and negative azimuth variations. This may be because the deep-rooted fault system separates lower and higher velocity blocks to the west and east of the boundary, respectively. As is shown in Figure 5, rays from the northeast and

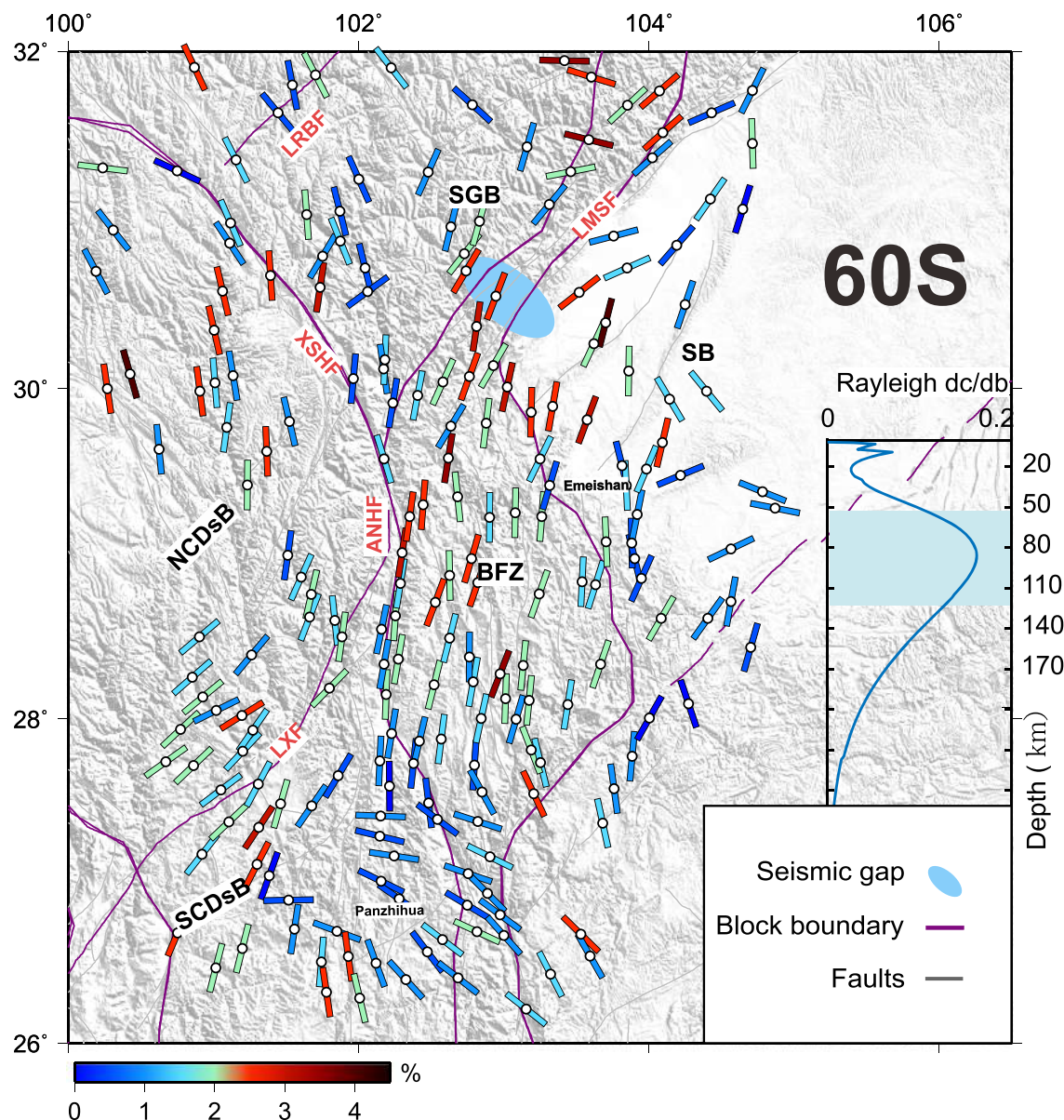


Figure 8. Results given in Figure 7 but for $T = 60$ s.

refracted at the boundary bend toward the normal of the boundary, producing positive azimuth anomalies to the west while near zero anomalies to the east.

In an elastic homogeneous medium, geometrical spreading is only related to the distance from the source and thus has a constant value along the same wavefront. However, in an inhomogeneous medium, waves can be focused and defocused. As is shown in Figures 5g–5i, geometrical spreading mainly reflects the influence of an inhomogeneous medium on waveform amplitudes. The positive geometrical spreading denotes that a waveform's amplitude is magnified (the wave is focused) while the negative geometrical spreading denotes that waves are attenuated (the wave is defocused) (Liang & Langston, 2009). The maximum amplitudes of geometrical spreading of $T = 20, 40$, and 60 s are roughly $8/1,000, 2/1,000$, and $1/1,000$ km, respectively. This may suggest that the crust is much more heterogeneous than the mantle and/or that short period waves are subject to higher medium attenuations or to more extensive focusing and defocusing. Distributions of geometrical spreading are roughly consistent with the wavefront and block boundary. On the same wavefront, the medium of high velocity (the medium may be more homogeneous) shows a

smaller magnitude of geometrical spreading (e.g., the Sichuan Basin relative to the Songpan-Ganzi block). For $T = 20$ s, geometrical spreading shows strong blockwise variations. However, based on events from different azimuths, the geometrical spreading also shows strong signs of path dependence. This may suggest that the amplitude variations are jointly affected by the medium beneath the stations and by the block boundaries on which waves reflect and deflect. For longer periods, negative geometrical spreading in the Songpan-Ganzi block is seemingly limited by the Longriba fault, Longmenshan fault, and Xianshuihe fault. Radiation patterns, which reflect the change of amplitude with the propagation direction, show a positive correlation with azimuth variation (Liang & Langston, 2009; Zhou et al., 2017).

4.2. Azimuthal Anisotropies in Various Periods

The azimuthal anisotropies of $T = 20, 40$, and 60 s are shown as 2-D maps in Figures 6–8. Their distributions are seemly divided by block boundaries or relative to the distribution of fault zones or the orientation of orogenic belts. Figure S7 shows statistics on the magnitude of anisotropies for different periods.

For $T = 20$ s (Figure 6), anisotropic magnitudes are roughly 1–3% (Figures 6 and S6a). The relatively large magnitudes distribute across multiple fault zones such as the BFZ, Xianshuihe fault, the northern part of Longmenshan fault, and Anninghe fault. A small magnitude appears in the southwestern SB, Panzhihua (located at the southern end of the Chuandian block), and southern part of Longmenshan fault. Fault perpendicular anisotropy appears in the northern part of the Longmenshan fault, the Lijiang-Xiaojin fault while fault parallel anisotropy appears in the southern part of the Longmenshan fault, Anninghe fault, BFZ, northern Chuandian subblock, Sichuan Basin, and Xianshuihe fault.

For $T = 40$ s (Figure 7), anisotropic magnitude is mostly valued at roughly 0.5–3%. The Panzhihua area still shows a small anisotropic magnitude (0.3–1.5%), but fast orientation changed from near N-S to NW-SE. Fast orientation along the Xianshuihe fault (NW-SE), Anninghe fault (S-N), north Chuandian subblock (NW-SE), and BFZ maintains fault parallel fast orientations, but anisotropy in BFZ is decline compared to $T = 20$ s. A significant number of stations show an almost 90° rotation of fast orientations for different periods. For example, fast orientation changed from fault perpendicular to fault parallel near the Lijiang-Xiaojin fault (NE-SW) and Longmenshan fault, and fast orientation changed from fault parallel to fault perpendicular near the Longriba fault (NW-SE).

For $T = 60$ s (Figure 8), anisotropy is similar to that of $T = 40$ s in most areas. The main difference is observed in the Xianshuihe fault and Xiaojin-Lijiang fault: Anisotropic magnitude is decline compare to $T = 40$ s; in the northern part of Longriba fault, fast orientation changed from near N-S to NE-SW.

We apply the bootstrap method to estimate the stability of anisotropic results in this study. We randomly resampled azimuth-dependent velocities 1,000 times to fit 1,000 anisotropic models and then evaluate the standard deviation (SD) of the M and φ of a given station; we used a parameter σ with combined SDs for stations to evaluate the overall errors:

$$\sigma = \frac{\text{std}\varphi}{90} + \frac{\text{std}M}{\max(M)},$$

and stations with $\sigma > 0.5$ are omitted in this study (see Tables S4–S6 and Figure S8), where $\text{std}\varphi$ is the SD of φ and $\text{std}M$ is the SD of M .

5. Discussion

5.1. The Reliability of Azimuthal Anisotropies Extracted by the WG Method

Synthetic data are used to test the reliability of the azimuthal anisotropy extracted by the WG. Here, we tested two cases with synthetic waveforms with or without 10% random noise. Figure S9a illustrates the procedure of the numerical experiments. We used the spectral element method (open source, refer to <https://geodynamics.org/cig/software/axisem>) to synthesize the theoretical seismic waveforms (Driel et al., 2014; Nissen-Meyer et al., 2004). The anisotropic model used in this study was defined by 36 1-D isotropic models in each 10° azimuth. For the anisotropic model with no random noise, each direction was only modified from the isotropic PREM model by adding velocity perturbations governed by equation (1) for the target layer (Mod1). The 36 sources from different directions are distributed around

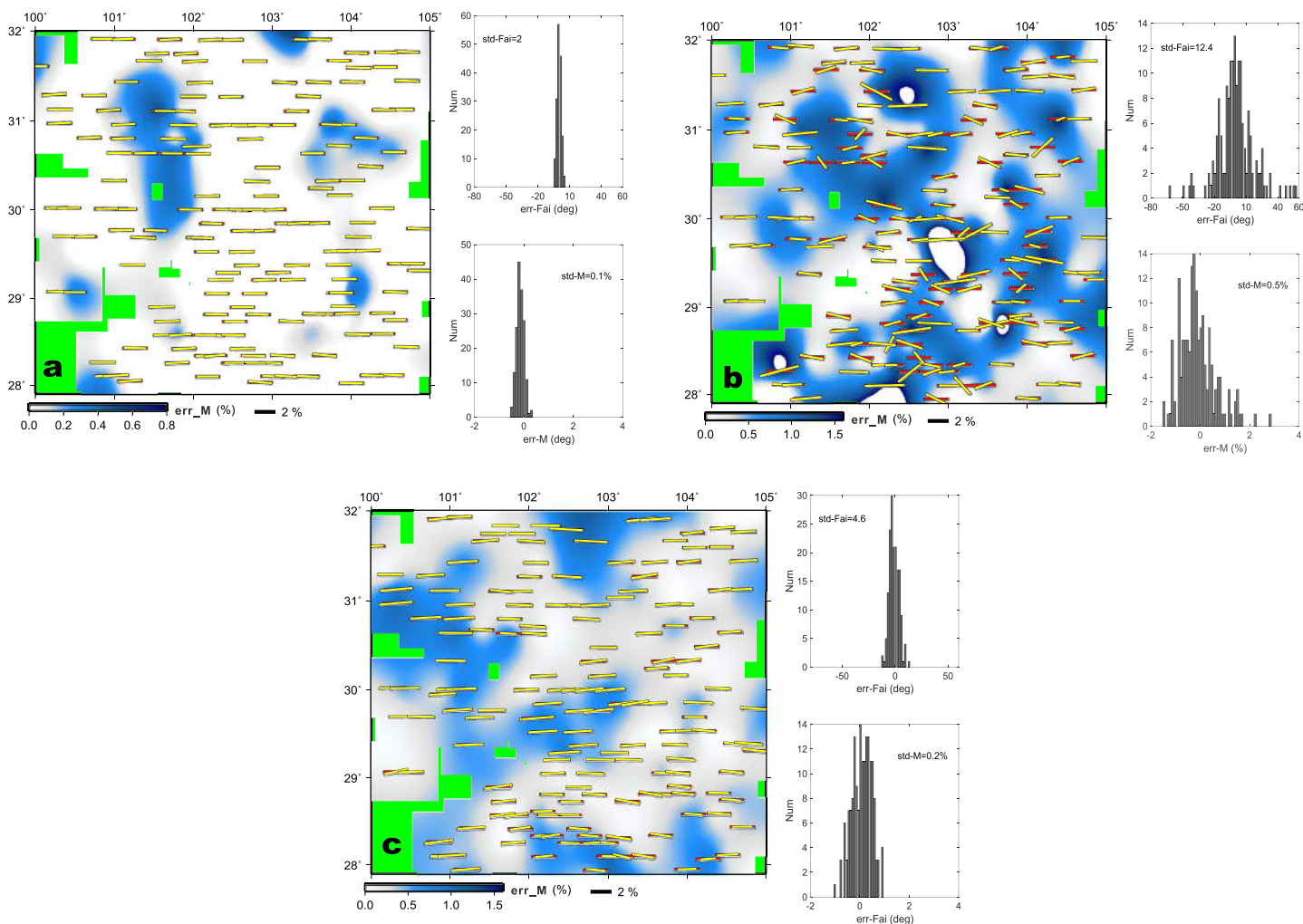


Figure 9. Numerical experiment results. (a) Result without adding random noise and wave scattering. The base map is the errors of anisotropic magnitude, the length and direction of bars denote the anisotropic magnitude and fast orientation, respectively, red bars represent the anisotropic model, and yellow bars represent the inverted result, two histograms on the right side indicate the error of fast orientation (top) and anisotropic magnitude (bottom); (b) same as (a) but the 10% random noise relate to Rayleigh wave crest was added to the synthetic waveform; (c) same as (b) but spatial-move average was applied to the results shown in (b).

the 166 stations (part of the TWSA, see Figure S9b). Based on the anisotropic model with no random noise, we generated Mod2 by adding 10% random noise (relative to the maximum crest of the Rayleigh wave) to the waveforms of Mod1. Anisotropic models with coefficients $[a, b]$ of $[-0.05, 0]$ are used to a period of 60 s (the results of other period tests are shown in Figure S10). In theory (equations (2) and (3)), anisotropic coefficients $[a, b]$ of $[-0.05, 0]$ have a fast orientation of 90° and have an anisotropic magnitude of 2.5% (assuming the isotropic velocity of the Rayleigh wave phase is 4 km/s in $T = 60$ s).

Following the same procedure for the real data processing, we obtained the phase velocity and anisotropy for the synthetic waveforms. Before anisotropic fitting, we take a spatial-move average on the phase velocity of Mod2 to generate the Mod3. Figure 9a shows the test results for Mod1; the average err-M (the error of anisotropic magnitude) is 0.15%, and the average err-Fai (errors of fast orientation) is 1.5° (Table 1). Figure 9b shows the test results for Mod2; the average err-M is 0.55%, and the average err-Fai is 12° (Table 1). Figure 11c shows the test results of Mod3; the average err-M is 0.34%, and the average err-Fai is 3.8° (Table 1). Relative to the Mod2, errors for the magnitude and fast orientation of the anisotropy decline by 0.34% and 8.2° , respectively.

Table 1
Numerical Experiment Results

	Average err-Fai (°)	Std-Fai (°)	Average err-M (%)	Std-M (%)
Mod1: No noise and no scatter	1.5	2	0.15	0.1
Mod2: 10% random noise	12	12.4	0.55	0.5
Mod3: 10% random noise and take spatial-move average	3.8	4.6	0.34	0.2

Note. Average err-Fai is the average error of fast orientation, Std-Fai is the standard deviation value of fast orientation error, Average err-M is the average error of anisotropic magnitude, and Std-M is the standard deviation value of anisotropic magnitude error.

In addition, we repeated the experiment for a homogeneous isotropic model to test the degree to which the anisotropy bias may be generated by irregular station distributions for the various cases with and without using the reducing velocity method. Figure S11a shows that when the reducing velocity method is not used, false anisotropies with scattering fast orientations and anisotropic magnitudes as large as 50% are observed. By contrast, when the reducing velocity method is used, Figure S11b shows that small anisotropic magnitudes (mostly smaller than 0.1%) and a relative homogeneous isotropic velocity are observed. Therefore, the experiment suggests that the reducing velocity is very important in reducing the bias caused by irregular arrays.

5.2. Comparisons to Other Studies

5.2.1. Methods for Extracting Anisotropies

Many techniques have been used to estimate radial and azimuthal anisotropy. Shear wave splitting is often used to estimate crust polarization anisotropy (Pms waves) and mantle radial anisotropy (SKS, SKKS) and has yielded numerous results (Chang et al., 2015; Chen et al., 2013; Crampin, 1985; Kong et al., 2018; Yang et al., 2018; Zheng et al., 2018; etc.). Shear wave splitting near earthquakes represents upper-middle crust anisotropy, but they are easily disturbed by the complexities of sources, multipath, and scattering (Lai et al., 2006); SKS splitting can yield stable anisotropies and is often attributed to the upper mantle anisotropic medium. Mattatall and Fouch (2007) suggest that SKS splitting in Parkfield is caused by crustal anisotropy. Yao et al. (2010) suggest that the lower crust may also make significant contributions to XKS splitting beneath the Tibetan Plateau. Thus, it is almost impossible to determine the exact contribution of the anisotropic layer by SKS splitting alone (Karato, 1998). Pms waves propagate only in the crust. Pn wave velocity is sensitive to temperatures and material compositions in the uppermost mantle and is the best way to estimate the history of mantle deformation (Liang et al., 2004; McNamara et al., 1997). For S wave splitting, results intuitively indicate the anisotropy under the station, but the signal-to-noise ratio is a critical influencing factor on splitting parameters because S waves are easily impacted by coda of P waves and slow S waves are easily impacted by coda of fast S waves (Sun et al., 2014). In addition, topography, tilted interfaces, scattering effects, and guided waves caused by faults also affect S wave splitting (Fang & Wu, 2009; Sun et al., 2014). The WG method takes amplitude variations into account and provides more information on wave propagation (see Figures 2, 3, and S1–S3). In addition, compared to the receiver function and SKS splitting method, it is applicable to almost full distance ranges. Using WG to estimate anisotropy was also different from the use of traditional surface wave tomography methods such as the two-station method, which needs earthquakes to align with the path linking two stations. For the WG method, the Rayleigh wave phase velocity from each earthquake is first estimated, and once a station's phase velocities from various back azimuths are found, we can easily and intuitively obtain the anisotropic parameters. The lateral resolution and reliability should be improved when the WG is applied to denser arrays. In addition to a velocity structure and azimuthal anisotropy, the WG may provide more medium information.

Other factors influencing anisotropic parameters extracted by WG include the following. (1) The dipping interface may cause Love and Rayleigh waves to interfere with each other (Xie et al., 2017; Zhou et al., 2017). Such mutual interference may cause the phase velocity to exhibit a fourth-order trigonometric function trend (Smith & Dahlen, 1973). (2) The density of phase velocity coverage on back azimuth also heavily influences the estimation of anisotropy. A lower density may overestimate the anisotropic magnitude and may generate a larger error on fast orientation. Therefore, stations with poor azimuthal coverage cannot be used for the fitting of anisotropic parameters. (3) Theoretically, the thicker the anisotropic layer, the more anisotropic magnitude is accumulated. Azimuth anisotropy in this study is considered a comprehensive effect of the sensitive layer of surface waves. The sensitive kernel curves of different frequencies (Figure S5) show that the sensitive layer of the low-frequency surface wave is much thicker than the high frequency although the sensitivity is relatively weak. Moreover, when a thick anisotropic layer contains media with inconsistent fast orientations at different depths, the overall anisotropic magnitude will be reduced due to stacking. (4) Similar to surface wave tomography based on finite frequency, backward scattering, healing wavefronts, and multiple paths also limit the robustness of WG in measuring the azimuth anisotropy (Bodin &

Maupin, 2008; Friederich et al., 2000; Lin & Ritzwoller, 2011a, 2011b; Tang et al., 2017; Wielandt, 1993). (5) The computation of spatial gradients is heavily reliant on the array density.

5.2.2. The Velocity Structure Along the Southeast Margin of the Tibetan Plateau

Fruitful achievements have been made along the southeast margin of the Tibetan Plateau. Yao et al. (2008, 2010) and Liu et al. (2014) found that strong contrasts of low velocity across the main fault zone (Longmenshan and Lijiang-Xiaojin faults, for example) and that lateral transfer occurred in the Xianshuihe fault and Lijiang-Xiaojin fault. Li et al. (2017) found that the Longmenshan fault, Xianshuihe fault, and Lijiang-Xiaojin fault form the boundary of density and electricity structure inverted by satellite gravity data and magnetotelluric sounding data. Low strong contrasts of Poisson's ratios are observed across Xianshuihe fault, Anninghe fault, and Lijiang-Xiaojin fault (He et al., 2017; Wang et al., 2009; Zhu et al., 2017). Our results (Figures 5a–5f) show that the Longmenshan fault and Lijiang-Xiaojin fault also serve as a sharp boundary that separates different blocks with strongly contrasting phase velocities of Rayleigh waves and azimuth variations in period bands centered at $T = 20$, 40, and 60 s. Therefore, we speculated that the Longmenshan fault and Lijiang-Xiaojin fault are deep-rooted faults that control the regional deformation of the lithosphere. The differential movement velocity observed between the north Chuandian subblock and south Chuandian subblock has caused the uplift of the north Chuandian subblock (~0.65 mm/a); the boundary of these two blocks (Lijiang-Xiaojin fault) exhibits sinistral strike slip (~6.4 mm/a) movement, the horizontal displacement of the Songpan-Ganzi block (1–2 mm/a), the blockage of the Sichuan Basin due to Longmenshan thrust uplift (1 mm/a), and the clockwise rotation of the Songpan-Ganzi block (3.9°/Ma) (Xu et al., 2003). The series of tectonic movements may be responsible for the wide distribution of the low-velocity zone beneath the Songpan-Ganzi block and north Chuandian subblock.

The south Chuandian subblock and BFZ (dashed ellipse of B4 in Figures 10–12) are influenced by the cooled Emeishan Large Igneous Province (Chung & Jahn, 1995; Guo et al., 2017; Xu et al., 2015) and present a relatively high velocity relative to the north Chuandian subblock and Songpan-Ganzi block for three periods. The velocity difference observed between the Songpan-Ganzi block (relatively high) and north Chuandian subblock decreases gradually from 0.3 km/s to zero as periods increase. This phenomenon may be associated with the control of the Xianshuihe fault over low velocities in the middle-upper crust of the plateau area.

The Rayleigh wave phase velocity results of this study are in good agreement with Yao et al. (2008, 2010) and Liu et al. (2014) though Liang and Langston (2009) concluded that the results of the two-station method are superior to those of WG for periods of less than 20 s. After fully considering the dense event and station coverage of the TWSA (which has unprecedented density in this region), our results for $T = 20$ s should be more reliable and reflect more details (Figures 5a–5c). As more large-scale dense arrays become available, WG's advantages in 3-D imaging are becoming increasingly obvious. Using the surface wave dispersion from WG to invert the 3-D S wave velocity in conjunction with other methods (such as receiver functions) may yield better results.

5.2.3. The Azimuthal Anisotropy Along the Southeast Margin of the Tibetan Plateau

Under the collision of the Indian-Eurasian plate and the blockage of strong blocks such as the North China Craton and Tarim Basin, the crust of the Tibetan Plateau is shortened and thickened. The plateau material has been extruding to the east and southeast, resulting in a series of complex and active tectonic activities in interior and surrounding areas of the plateau (Chen et al., 2000; Houseman & England, 1993; Xu et al., 1999). With differential resistance, the north Chuandian subblock and Songpan-Ganzi block are separated by the sinistral strike-slip Xianshuihe fault. To develop further understanding of the geodynamic characteristics of the southeast margin of the Tibetan Plateau, we estimated azimuthal anisotropy parameters of the TWSA based on the WG method. Our anisotropic fast orientations (Figures 6–8 and 10–12) show a strong correlation with the strikes of the fault system and orogenic belts. The anisotropy magnitudes range between 1% and 3% and are consistent with those calculated in previous studies (Chen et al., 2013; Friederich, 2003; Lebedev & Nolet, 2003; Legendre et al., 2015; Pandey et al., 2015; Yao et al., 2010; Zheng et al., 2018).

As shown in Figure 6, the fast orientations of anisotropies for $T = 20$ s are mostly parallel to regional or local faults. Figure 10 compares the fast orientation determined by WG (called FO1) with that determined from Pms phases for the same array by Zheng et al. (2018) (called FO2). Because both methods are station-based, the difference in fast orientations can be found by finding the angular differences of the two vectors. The rose diagram presented in Figure 10 shows the statistics of angular differences between FO1 (with an anisotropic magnitude larger than 1.5%) and FO2 (with a delay time larger than 0.15 s). As

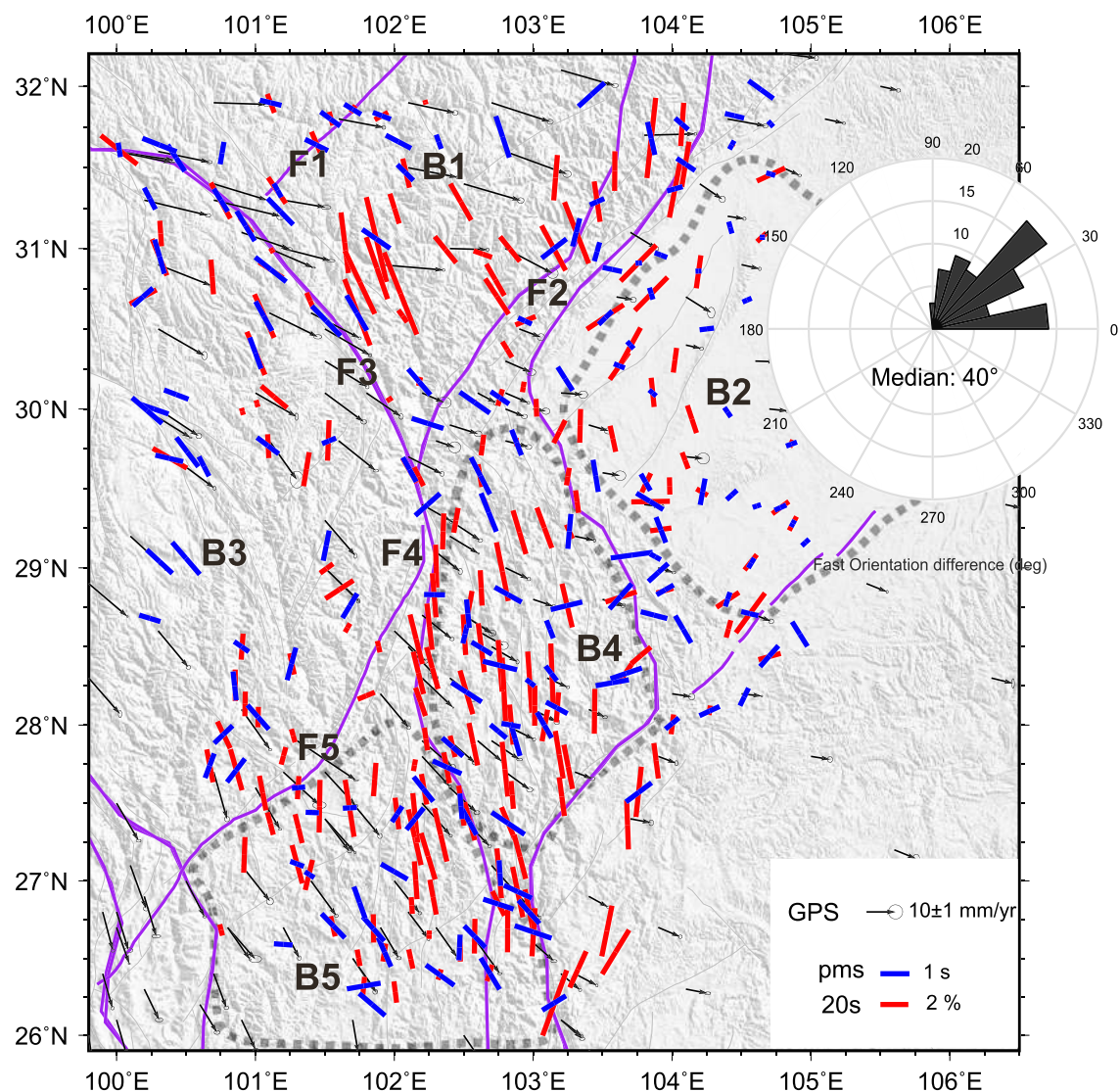


Figure 10. Comparisons of the observed Pms wave splitting (blue bars taken from Zheng et al., 2018) to azimuthal anisotropy at $T = 20$ s estimated by WG (red bars). B1: Songpan-Ganzi block; B2: Sichuan Basin; B3: north Chuandian block; B4: boundary fault zone; B5: south Chuandian block; F1: Longriba fault; F2: Longmenshan fault; F3: Xianshuihe fault; F4: Anning He fault; F5: Lijiang-Xiaojin fault. Rose diagrams on the right indicate the statistics of fast orientation differences between those based on WG ($T = 20$ s, and $M > 1.5\%$) and those based on Pms phases (delay time larger than 0.15 s) while “median” is the median value of the fast orientation difference.

can be observed, the median of angular differences is around 40° , and the two results are more consistent in the plateau area, which shows active tectonic activity and a low velocity (e.g., the Songpan-Ganzi block, north Chuandian subblock, and Xianshuihe fault).

Compared to the surface velocity extracted from GPS data (Zhao et al., 2015), the fast orientations of anisotropies are more consistent with the strikes of the local faults and have a systematic angular difference with surface velocity (the BFZ, for example). The surface velocity extracted from the GPS data represents current tectonic activity, and azimuthal anisotropy may reflect relics of historical tectonic activity.

For $T = 40$ s, the rose diagram presented in Figure 11 shows that the majority of angular differences are less than 25° . The phase velocity of the Rayleigh waves at $T = 40$ s is more sensitive to depths of 30–90 km (Figure S5). Given the thinner crust beneath the Sichuan Basin and thicker crust in the eastern Tibetan Plateau, anisotropies of $T = 40$ s mainly represent the lower crust in the plateau area and the uppermost mantle of the Sichuan Basin. As a result, the anisotropy of $T = 40$ s determined by the WG method for the eastern Tibetan

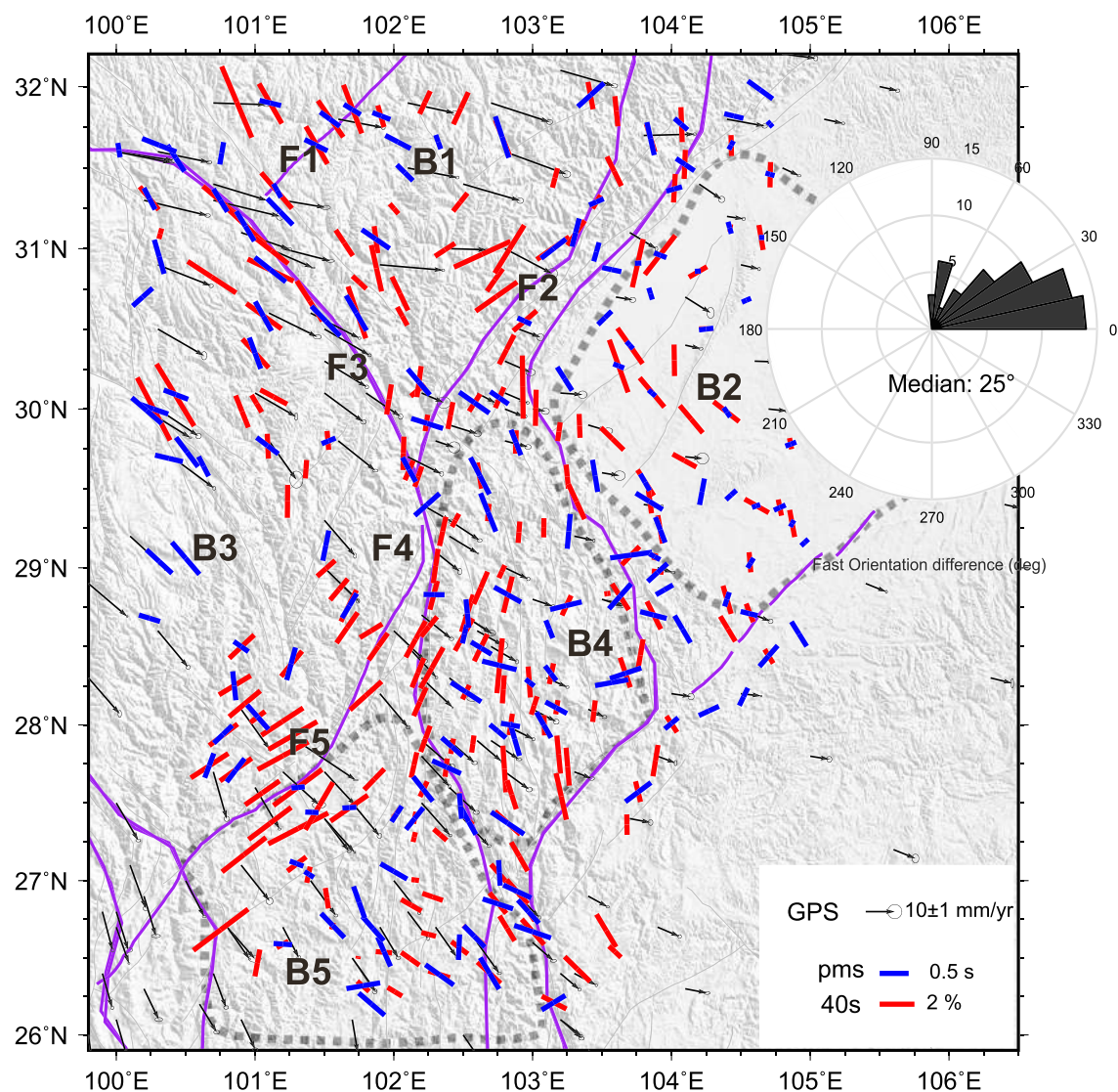


Figure 11. Results shown in Figure 10 but for $T = 40$ s.

Plateau area and Sichuan Basin is consistent with the results derived from Pms waves (Zheng et al., 2018). In addition, the results generated from Pms phases are more consistent with the anisotropy of $T = 40$ s than with the anisotropy of $T = 20$ s. This may indicate that the anisotropy derived from Pms phases by Zheng et al. (2018) mostly originates from the lower crust, the depth of which both methods are sensitive.

Chen et al. (2013) measured radial anisotropy by analyzing the shear wave splitting of Pms phases in a similar area and where the average splitting time is roughly 0.19 s; Zheng et al. (2018) measured the azimuthal anisotropy of Pms phases and found an average delay time of approximately 0.42 s. This discrepancy may suggest that the multiple-event stacking technique used by Chen resulted a shorter delay time (Kong et al., 2018). Our method seems to be consistent with the magnitude given by Zheng et al. (2018). The average anisotropic magnitudes of $T = 40$ s and $T = 20$ s are roughly 1.77% and 2.3%, respectively. If the anisotropic layers corresponding to these two periods are 35 and 25 km, respectively, then our anisotropic magnitude is approximately 0.35 s, which is closer to what is given by Zheng et al. (2018).

An anisotropy of $T = 60$ s mainly represents the upper mantle. Our results are in good agreement with the XKS splitting results of previous studies (collected by <http://splitting.gm.univmontp2.fr/DB/index.html> and Chang et al., 2015) for some area as shown in the rose diagram in Figure 12. This may suggest that the

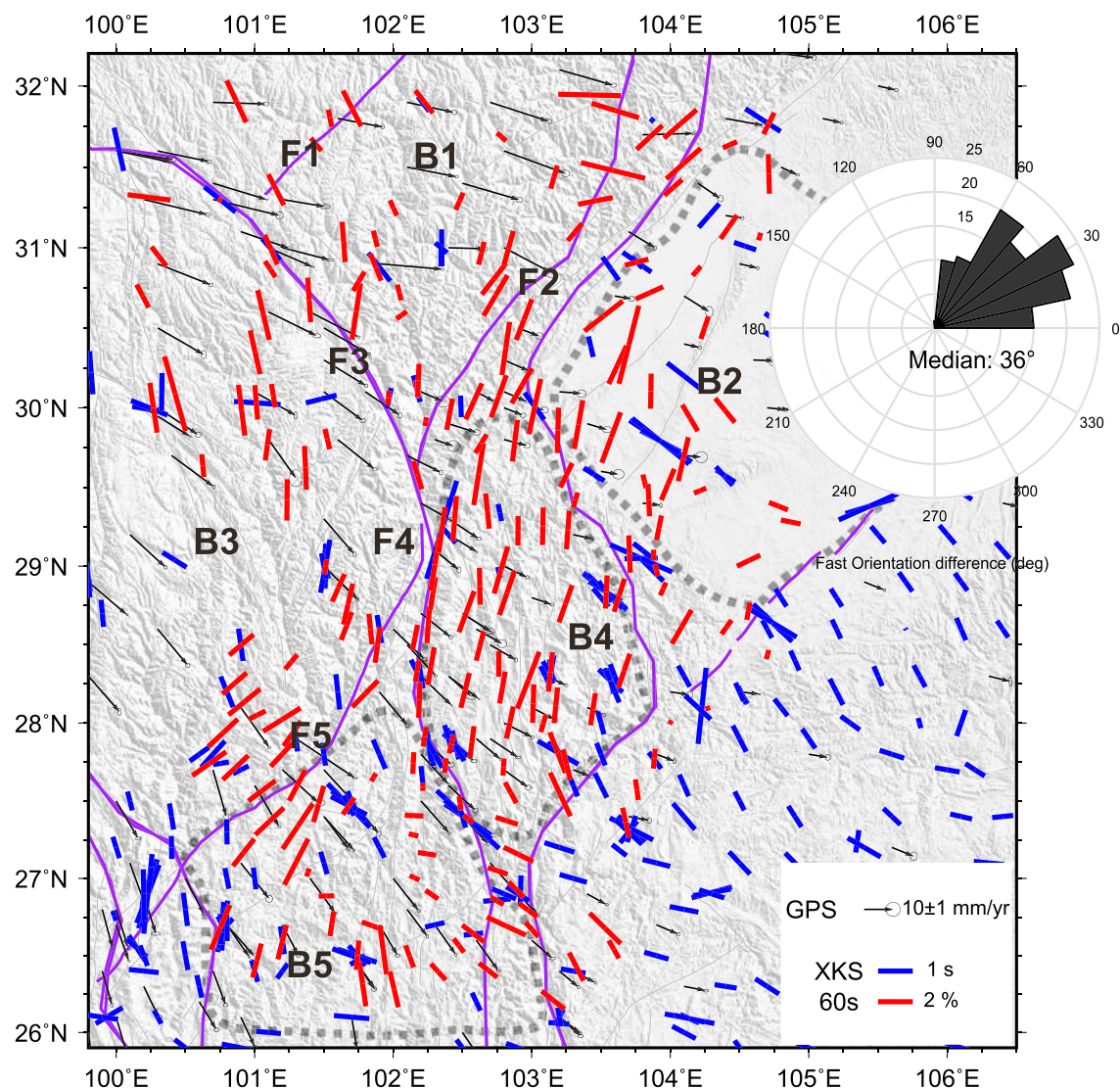


Figure 12. Comparison of the observed XKS wave splitting (yellow bars taken from Chang et al., 2015, and blue bars collected from <http://splitting.gm.univmontp2.fr/DB/index.html>) to azimuthal anisotropy at $T = 40$ s estimated by WG (red bars). B1: Songpan-Ganzi block; B2: Sichuan Basin; B3: north Chuandian block; B4: boundary fault zone; B5: south Chuandian block; F1: Longriba fault; F2: Longmenshan fault; F3: Xianshuuhe fault; F4: Anning He fault; F5: Lijiang-Xiaojin fault. Rose diagrams on the right indicate the statistics of fast orientation differences between those based on WG ($T = 60$ s, and $M > 1.5\%$) and those based on XKS phases (delay time larger than 0.25 s) while “median” is the median value of the fast orientation difference.

anisotropy measured by SKS splitting mainly originates from the upper mantle in this area. In the XSHF, ANHF, XLF, and SCDsB, the fast orientation of XKS splitting is generally consistent with the fast orientation of $T = 60$ s. The BFZ has a nearly north-south fast orientation and is parallel to the local fault zone and orogenic belt, and it is consistent with the phase velocity anisotropy given by Yao et al. (2010) but differing from the fast orientation of the XKS.

For $T = 20, 40$, and 60 s, the fast orientation of the BFZ is almost parallel to the orogenic belt and internal small fault zone for all three periods of this study. This may suggest that the anisotropies observed in these regions originate from the ancient internal deformation of the lithosphere (e.g., ancient orogenic events associated with fold uplift and strike-slip deformation). The fast orientation of anisotropies from XKS and Pms, the direction of maximum compressive stresses (Yang et al., 2018), and surface movement detected by GPS are aligned at nearly NW-SE, and they are systematically different from fault strikes and orogenic belts. The surface movement direction (Zhao et al., 2015) and maximum compressive stresses direction

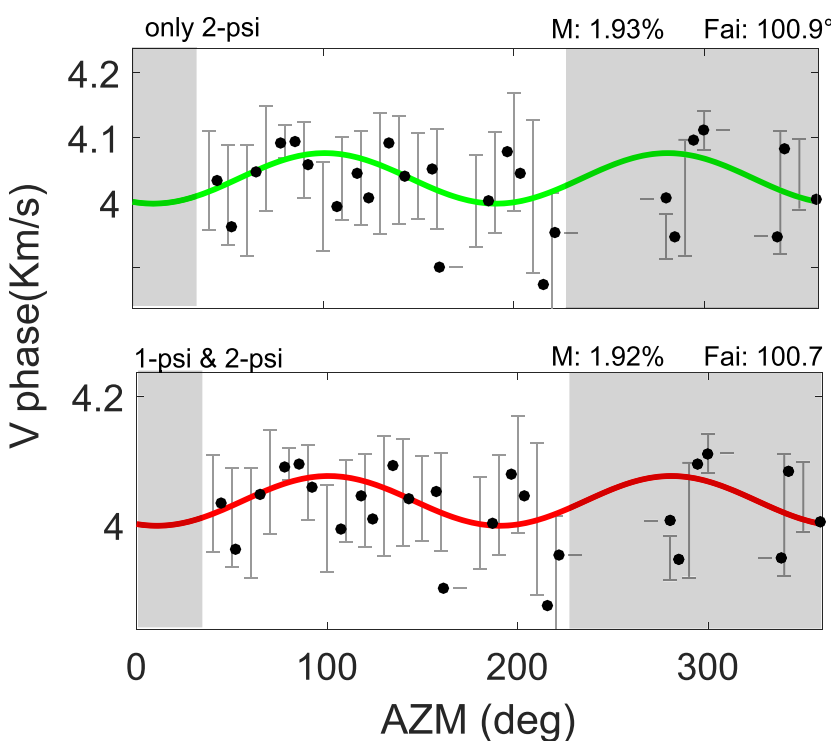


Figure 13. Comparison of the anisotropic fitting with and without the 1-psi terms for the station KZG05 in $T = 60$ s. The green curved line denotes the fitted curve governed by equation (1), and the red curved line denotes the fitted curve governed by equation (4). The gray bars denote the error bars of azimuthal dependence phase velocity; black dots are the median velocity in every 10° . Gray areas mark the back azimuth range with low density of fitting data. M is anisotropic magnitude, and Fai is the anisotropic fast orientation.

(Yang et al., 2017, 2018) inverted by focal mechanisms carry information on current tectonic movement, and they may not be affected by ancient tectonic events as much as the fast orientation of anisotropies determined by the WG method. In addition, considering the difference in periods observed between the surface wave (long periods) and S wave (short periods), the anisotropy of the long-period surface wave may be more sensitive to macroscopic structures created by the deformation of the lithosphere while short-period S wave splitting is more sensitive to local stresses or the microscopic structure. Differences between the results derived from the WG method and from methods based on Pms and XKS phases, however, may be due to the different ray paths considered as well. However, a thorough investigation is needed to address this possibility.

5.2.4. Comparison of Azimuthal Anisotropy in Two Different Fitting Models

In previous studies, it is a common practice for the anisotropic fitting model only to contain the second-order term (2-psi) (Yao et al., 2010; Zheng et al., 2018), but if take the influence of backward scattering on the long-period Rayleigh wave into account, the anisotropic fitting model needs to contain the first-order (1-psi) term, as suggested by Lin and Ritzwoller (2011a, 2011b). Given the fitting model as below:

$$v = \bar{v} + a\cos(2\theta) + b\sin(2\theta) + c\cos(\theta) + d\sin(\theta), \quad (4)$$

where \bar{v} is the isotropic velocity, a and b are the coefficients of 2-psi terms, and c and d are the coefficients of 1-psi terms. In this section, we fitted both equations (1) and (4) with real data from 0° to 360° to evaluate the degree of influence of the 1-psi term on the parameters of the 2-psi terms.

Figure 13 compares the fitting results of 2-psi terms of the station KZG05 in two different fitting models; the differences of fast orientation and anisotropic magnitude are roughly 0.01% and 0.2° , respectively, for $T = 60$ s. Figure 14 shows the histograms of differences of two sets of anisotropic parameters for all station at $T = 20, 40$, and 60 s. We noted that, for most stations, the differences between the two different anisotropic fitting models are small, but for some stations they are still large. So it is better to take the back-scattering

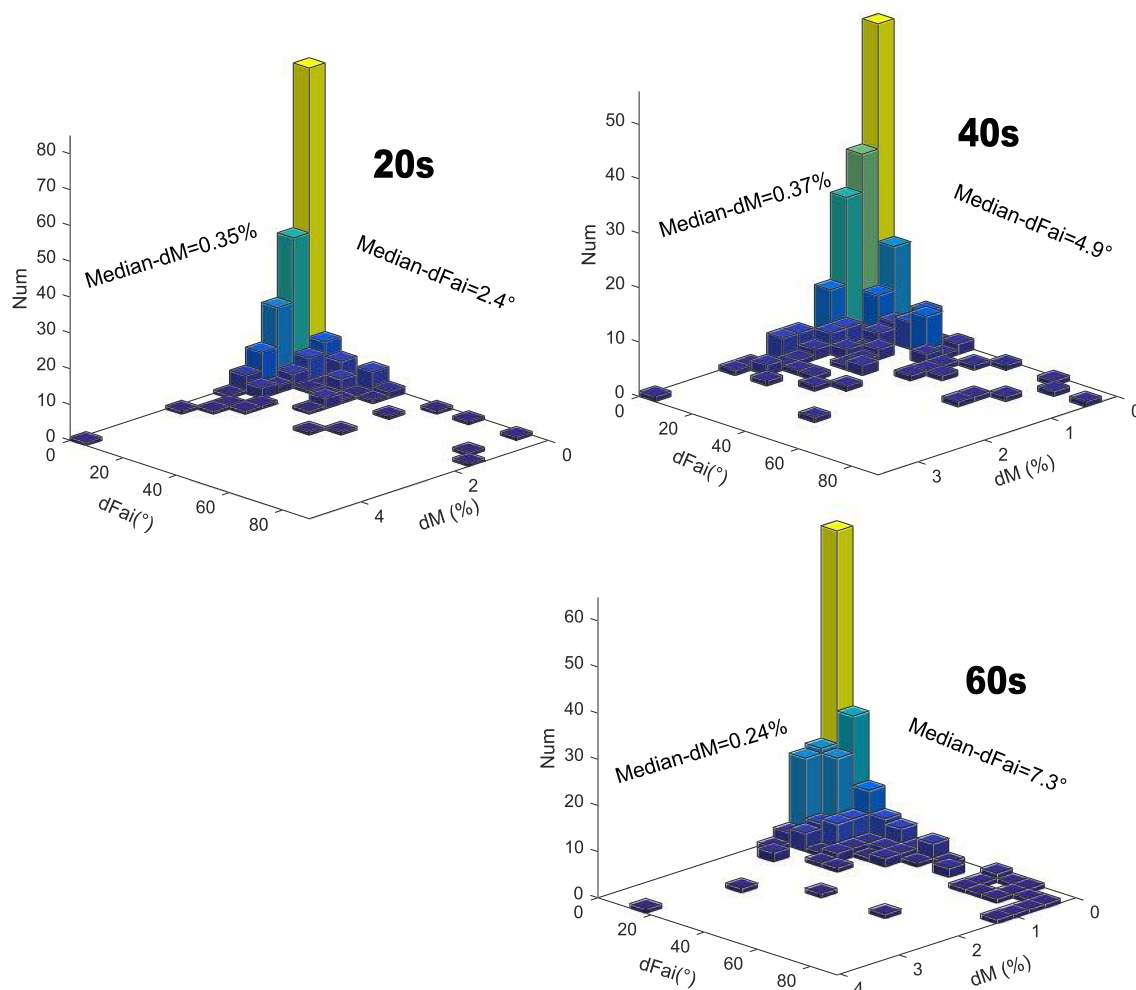


Figure 14. Histogram for the differences of two anisotropic parameters between two anisotropic fitting models (equations (1) and (4)) in three periods. $D - M$ (%) is the difference of anisotropic magnitude, and $D - Fai$ (deg) is the difference of fast orientation; median – $dFai$ is the median value of fast orientation differences, and median – dM is the median value of anisotropic magnitude differences.

effects into account when a better azimuthal coverage is achieved. But in this study, the uneven azimuthal coverage of phase velocity mostly appears in $230\text{--}360^\circ$ and $0\text{--}30^\circ$ in this study area (Figure 2 and gray areas in Figure 14); it is a challenge to fit the 1-psi term which requires the relatively even azimuthal coverage for all angles. In addition, the median value of anisotropic magnitude differences (median – dM) and fast orientation difference (median – $dFai$) are roughly 0.35% and 2.4° , 0.37% and 4.9° , and 0.24% and 7.3° for $T = 20, 40$, and 60 s, respectively; these differences are less than the errors showed in Tables S4–S6 and Figure S8. Therefore, in this study, we only fitted the 2-psi term in $0\text{--}180^\circ$ (see section 3 for details) to increase the azimuthal coverage.

6. Conclusion

In this study, we used the WG method with a plane wave assumption to calculate the azimuthal anisotropy of Rayleigh wave phase velocity for three period bands. Based on subtle differences in the waveforms of sub-arrays, we obtained isotropic phase velocity and azimuthal anisotropy parameters for various periods for WSTA stations. The study may provide further constraints on the lithospheric deformation of the southeastern margin of the Tibetan Plateau. Our main conclusions are as follows:

1. On the basis of dense arrays, WG fully considers the waveform difference between stations to find the phase velocity of various back azimuths and then used to fitting azimuthal anisotropy

parameters. In addition, WG is found to be stable in extracting azimuthal anisotropy, especially for fast orientation.

2. The Lijiang-Xiaojin fault and Longmenshan fault appear to form a deep-rooted strong boundary at the lithosphere scale. The fault system separates a low-velocity zone to the northwest and a high-velocity zone to the southeast. They also serve as a boundary of anisotropic structures.
3. The anisotropy of the Longriba and Lijiang-Xiaojin faults for different periods reveals a more complex geologic setting in the collision zone.
4. In the BFZ, anisotropic fast orientation estimated by WG shows systematic angular differences from the surface movement direction derived from the GPS data, and maximum compressive stress inverted by focal mechanisms may suggest that anisotropies observed in this region originated from the ancient internal coherent deformation of the lithosphere.

However, we must also point out that, in this study, only velocity and azimuthal anisotropies are obtained for certain period bands, and the sensitivity of each period band samples a wide depth range beneath each station. Therefore, caution should be taken while interpreting these data. A 3-D inversion based on dispersion curves constructed from a series of period bands will be developed and will be a focus of our further work.

Acknowledgments

Critical reviews by Professor de Ridder, Dr Yihai Yang, and another anonymous reviewer significantly improved the manuscript. Thanks Professor Yun Chen and Dr Tuo Zheng for providing the results of Pms splitting. Waveform data were provided by the China Seismic Array Data Management Center of the Institute of Geophysics, China Earthquake Administration (<http://www.chinarraydmc.cn/products/index>). This study was partially supported by the National Key R&D Program of China (Grant 2018YFC1503401) and the Chinese National Science Foundation (Grants 41374058 and 41674059). The synthesized data were computed by AxisEM (<https://geodynamics.org/cig/software/axisem>). XKS splitting results for the studied region were collected online (from <http://splitting.gm.univmontp2.fr/DB/index.html>).

References

- Agius, M. R., & Lebedev, S. (2017). Complex, multi-layered azimuthal anisotropy beneath Tibet: Evidence for co-existing channel flow and pure-shear crustal thickening. *Geophysical Journal International*. <https://doi.org/10.1093/gji/ggx266>
- Ali, J., Fitton, J., & Herzberg, C. (2010). Emeishan large igneous province (SW China) and the mantle-plume up-doming hypothesis[J]. *Journal of the Geological Society*, 167(5), 953–959. <https://doi.org/10.1144/0016-7649-2009-129>
- Ali, J. R., Thompson, G. M., Zhou, M., & Song, X. (2005). Emeishan large igneous province, SW China[J]. *Lithos*, 79(3), 475–489. <https://doi.org/10.1016/j.lithos.2004.09.013>
- Babuska, V., & Cara, M. (1991). Anisotropy in deeper parts of the Earth[M]//Seismic anisotropy in the earth. Springer Netherlands. https://doi.org/10.1007/978-94-011-3600-6_6
- Backus, G. E. (1965). Possible forms of seismic anisotropy of the uppermost mantle under oceans[J]. *Journal of Geophysical Research*, 70 (14). <https://doi.org/10.1029/JZ070i014p03429>
- Bai, D., Unsworth, M. J., Meju, M. A., Ma, X., Teng, J., Kong, X., et al. (2010). Crustal deformation of the eastern Tibetan plateau revealed by magnetotelluric imaging[J]. *Nature Geoscience*, 3(5), 358–362. <https://doi.org/10.1038/ngeo830>
- Bodin, T., & Maupin, V. (2008). Resolution potential of surface wave phase velocity measurements at small arrays[J]. *Geophysical Journal of the Royal Astronomical Society*, 172(2), 698–706. <https://doi.org/10.1111/j.1365-246X.2007.03668.x>
- Boness, N. L. (2004). Stress-induced seismic velocity anisotropy and physical properties in the SAFOD Pilot Hole in Parkfield, CA[J]. *Geophysical Research Letters*, 31(15), L15S17. <https://doi.org/10.1029/2003gl019020>
- Burchfiel, B. C., Zhiliang, C., Yupinc, L., & Royden, L. H. (1995). Tectonics of the Longmen Shan and adjacent regions, central China. *International Geology Review*, 37(8), 661–735. <https://doi.org/10.1080/00206819509465424>
- Ceylan, S., Ni, J., Chen, J. Y., Zhang, Q., Tilman, F., & Sandvol, E. (2012). Fragmented Indian plate and vertically coherent deformation beneath eastern Tibet[J]. *Journal of Geophysical Research Solid Earth*, 117(B11). <https://doi.org/10.1029/2012JB009210>
- Chang, L. J., Ding, Z. F., & Wang, C. Y. (2015). Upper mantle anisotropy beneath the southern segment of North-South tectonic belt, China[J]. *Chinese Journal of Geophysics*, 58(11), 4052–4067. <https://doi.org/10.6038/cjg2015114>
- Chen, Y., Zhang, Z., Sun, C., & Badal, J. (2013). Crustal anisotropy from Moho converted Ps wave splitting analysis and geodynamic implications beneath the eastern margin of Tibet and surrounding regions[J]. *Gondwana Research*, 24(3–4), 946–957.
- Chen, Z., Burchfiel, B. C., Liu, Y., King, R. W., King, L. H., Tang, W., et al. (2000). Global Positioning System measurements from eastern Tibet and their implications for India/Eurasia intercontinental deformation[J]. *Journal of Geophysical Research Solid Earth*, 105(B7), 16,215–16,227. <https://doi.org/10.1029/2000jb900092>
- Cheng, J., Xi-Wei, X. U., & Gan, W. J. (2012). Block model and dynamic implication from the earthquake activities and crustal motion in the southeastern margin of Tibetan Plateau[J]. *Chinese Journal of Geophysics*, 55(4), 1198–1212. <https://doi.org/10.6038/j.issn.0001-5733.2012.04.016>
- ChinArray (2006). China Seismic Array waveform data. China Earthquake Administration. <https://doi.org/10.12001/ChinArray.Data>.
- Chung, S. L., & Jahn, B. (1995). Plume-lithosphere interaction in generation of the Emeishan flood basalts at the Permian-Triassic boundary[J]. *Geology*, 23(10), 889. 108(9). [https://doi.org/10.1130/0091-7613\(1995\)023<0889:PLIGO>2.3.CO;2](https://doi.org/10.1130/0091-7613(1995)023<0889:PLIGO>2.3.CO;2)
- Crampin, S. (1966). Higher-mode seismic surface waves from atmospheric nuclear explosions over Novaya Zemlya[J]. *Journal of Geophysical Research*, 71(12), 2951–2958. <https://doi.org/10.1029/JZ071i012p02951>
- Crampin, S. (1985). Evaluation of anisotropy by shear-wave splitting[J]. *Geophysics*, 50, 142–152. <https://doi.org/10.1190/1.1441824>
- Crampin, S., Booth, D. C., Evans, R., et al. (1991). Comment on “Quantitative measurements of shear wave polarizations at the Anza Seismic Network, southern California: Implications for shear wave splitting and earthquake prediction” by Richard C. Aster, Peter M. Shearer, and Jon Berger[J]. *Journal of Geophysical Research: Solid Earth*, 96(B4). <https://doi.org/10.1029/90JB02453>
- Crampin, S., Evans, R., Üçer, B., Doyle, M., Davis, J. P., Yegorkina, G. V., & Miller, A. (1980). Observations of dilatancy-induced polarization anomalies and earthquake prediction. *Nature*, 286(5776), 874–877. <https://doi.org/10.1038/286874a0>
- De Ridder, S., & Curtis, A. (2017). Seismic gradiometry using ambient seismic noise in an anisotropic Earth[J]. *Geophysical Journal International*, 209(2), 1168–1179. <https://doi.org/10.1093/gji/ggx073>
- Deng, Q. D., Zhang, P. Z., Ran, Y. K., Yang, X. P., Min, W., & Chen, L. C. (2003). Active tectonics and earthquake activities in China. *Earth Science Frontiers*, 10(SUPP), 66–73. <http://search.cnki.net/down/default.aspx?filename=DXQY2003S1011&dbcode=CJFD&year=2003&dflag=pdfdown>

- Driel, M. V., Fournier, A., Auer, L., Hosseini, K., Nissen-Meyer, T., Hempel, S., et al. (2014). AxiSEM: Broadband 3-D seismic wavefields in axisymmetric media. *Solid Earth*, 5(1), 265–319. <https://doi.org/10.5194/se-5-425-2014>
- Edme, P., & Yuan, S. (2016). Local dispersion curve estimation from seismic ambient noise using spatial gradients[J]. *Interpretation*, 4(3). <https://doi.org/10.1190/INT-2016-0003.1>
- Fan, L. P., Wu, J. P., & Fang, L. H. (2015). Teleseismic P wave tomography in the southeast margin of the Tibetan Plateau[J]. *CT Theory and Applications*, 24(2): 209–223. (in Chinese). <https://doi.org/10.15953/j.1004-4140.2015.24.02.07>
- Fang, L. H., & Wu, J. P. (2009). Effect s of dipping boundaries and anisotropic media on receiver functions. *Progress in Geophysics (in Chinese)*, 24(1):42-50. [https://doi.org/10.1016/S1874-8651\(10\)60080-4](https://doi.org/10.1016/S1874-8651(10)60080-4)
- Friederich, W. (2003). The S-velocity structure of the East Asian mantle from inversion of shear and surface waveform. *Geophysical Journal International*, 153, 88–102. <https://doi.org/10.1046/j.1365-246X.2003.01869.x>
- Friederich, W., Hunzinger, S., & Wielandt, E. (2000). A note on the interpretation of seismic surface waves over three-dimensional structures[J]. *Geophysical Journal International*, 143(2), 335–339. <https://doi.org/10.1046/j.1365-246X.2000.01241.x>
- Guo, B., Liu, Q. Y., Chen, J. H., Liu, L.-S., Li, S.-C., Li, Y., et al. (2009). Teleseismic P-wave tomography of the crust and upper mantle in Longmenshan area, west Sichuan. *Chinese Journal of Geophysics (in Chinese)*, 52(2), 346–355. <https://doi.org/10.1785/0120080023>
- Guo, X., Chen, Y., Li, S. D., Deng, Y.-F., Xu, T., Li, W., & Tan, P. (2017). Crustal shear-wave velocity structure and its geodynamic implications beneath the Emeishan large igneous province. *Chinese Journal of Geophysics (in Chinese)*, 60(9), 3338–3351. <https://doi.org/10.6038/cjg20170906>
- He, F., Liang, C., Yang, Y., Fang, L., & Su, J. (2017). The crust structure of the unruptured segment between Wenchuan and Lushan Earthquakes revealed by Receiver Functions. *Chinese Journal of Geophysics*, 60(6), 2130–2146. <https://doi.org/10.6038/cjg20170609>
- Hess, H. (1964). Seismic Anisotropy of the Uppermost Mantle under Oceans. *Nature*, 203, 629–631. <https://doi.org/10.1038/203629a0>
- Houseman, G., & England, P. (1993). Crustal thickening versus lateral expulsion in the Indian-Asian continental collision. *Journal of Geophysical Research*, 98(B7), 12,233–12,249. <https://doi.org/10.1029/93JB00443>
- Huang, Z., Wang, L., Xu, M., & Zhao, D. (2018). P-wave anisotropic tomography of the SE Tibetan Plateau: Evidence for the crustal and upper-mantle deformations. *Journal of Geophysical Research Solid Earth*. <https://doi.org/10.1029/2018JB016048>
- Hubbard, J., & Shaw, J. H. (2009). Uplift of the Longmen Shan and Tibetan plateau, and the 2008 Wenchuan (M=7.9) earthquake. *Nature*, 458, 194–197. <https://doi.org/10.1038/nature07837>
- Hubbard, J., Shaw, J. H., & Klinger, Y. (2010). Structural setting of the 2008 Mw 7.9 Wenchuan, China, earthquake. *Bulletin of the Seismological Society of America*, 100(5B), 2713–2735. <https://doi.org/10.1785/0120090341>
- Jin, G., & Gaherty, J. B. (2015). Surface wave phase-velocity tomography based on multichannel cross-correlation[J]. *Geophysical Journal International*, 201(3), 1383–1398. <https://doi.org/10.1093/gji/ggv079>
- Karato, S. (1998). Seismic anisotropy in the deep mantle and the geometry of mantle convection. *Pure and Applied Geophysics*, 151, 565–587. <https://doi.org/10.1007/s00240050130>
- Klemperer, S. L. (2006). Crustal flow in Tibet: Geophysical evidence for the physical state of Tibetan lithosphere, and inferred patterns of active flow. *Geological Society of London, Special Publication*, 268, 265–308. <https://doi.org/10.1144/GSL.SP.2006.268.01.03>
- Kong, F., Wu, J., Liu, K. H., & Gao, S. S. (2016). Crustal anisotropy and ductile flow beneath the eastern Tibetan Plateau and adjacent areas. *Earth and Planetary Science Letters*, 442, 72–79. <https://doi.org/10.1016/j.epsl.2016.03.003>
- Kong, F., Wu, J., Liu, L., Liu, K. H., Song, J., Li, J., & Gao, S. S. (2018). Azimuthal anisotropy and mantle flow underneath the southeastern Tibetan Plateau and northern Indochina Peninsula revealed by shear wave splitting analyses. *Tectonophysics*, 68–78. <https://doi.org/10.1016/j.tecto.2018.09.013>
- Lai, Y. G., Liu, Q. Y., Chen, J. H., Liu, J., Li, S.-C., Guo, B., & Huang, Z.-B. (2006). Shear wave splitting and the features of the crustal stress field in the capital circle[J]. *Chinese Journal of Geophysics*, 49(1), 157–166. <https://doi.org/10.1002/cjg2.823>
- Langston, C. A. (2007a). Spatial gradient analysis for linear seismic arrays. *Bulletin of the Seismological Society of America*, 97(1B), 265–280. <https://doi.org/10.1785/0120060100>
- Langston, C. A. (2007b). Wave gradiometry in the time domain. *Bulletin of the Seismological Society of America*, 97(3), 926–933. <https://doi.org/10.1785/0120060152>
- Langston, C. A. (2007c). Wave gradiometry in two dimensions. *Bulletin of the Seismological Society of America*, 97(2), 401–416. <https://doi.org/10.1785/0120060138>
- Langston, C. A., & Ayele, M. M. (2016). Vertical seismic wave gradiometry: Application at the San Andreas Fault Observatory at depth. *Geophysics*, 81(3), D233–D243. <https://doi.org/10.1190/geo2015-0404.1>
- Langston, C. A., Bodin, P., Powell, C. A., Withers, M., Horton, S., & Mooney, W. D. (2006). Explosion source strong ground motions in the Mississippi embayment. *Bulletin of the Seismological Society of America*, 96(3), 1038–1054. <https://doi.org/10.1785/0120050105>
- Lebedev, S., & Nolet, G. (2003). Upper mantle beneath Southeast Asia from S velocity tomography. *Journal of Geophysical Research*, 108, 2048. <https://doi.org/10.1029/2000JB000073>
- Legendre, C. P., Deschamps, F., Zhao, L., & Chen, Q. F. (2015). Rayleigh-wave dispersion reveals crust-mantle decoupling beneath eastern Tibet. *Scientific Reports*, 5(1), 16644. <https://doi.org/10.1038/srep16644>
- Li, C., Van der Hilst, R. D., Meltzer, A. S., & Engdahl, E. R. (2008). Subduction of the Indian lithosphere beneath the Tibetan plateau and Burma. *Earth and Planetary Science Letters*, 274, 157–168. <https://doi.org/10.1016/j.epsl.2008.07.016>
- Li, J., Wang, X. B., Li, D. H., Qin, Q.-Y., Zhang, G., Zhou, J., et al. (2017). Characteristics of the lithosphere physical structure in eastern margin of Qinghai-Tibet plateau and their deep tectonic implications. *Chinese Journal of Geophysics (in Chinese)*, 60(6), 2500–2511. <https://doi.org/10.6038/cjg20170637>
- Li, X., Yao, H. J., Li, Y., & Liu, Q. Y., (2015). Effect of off-great-circle propagation on surface wave phase velocity tomography in western Sichuan. *Acta Seismologica Sinica*, 37(1), 15–28. <https://doi.org/10.11939/jass.2015.01.002>
- Liang, C., & Langston, C. A. (2009). Wave gradiometry for USArray: Rayleigh waves. *Journal of Geophysical Research: Solid Earth*, 114(B2). <https://doi.org/10.1029/2008jb005918>
- Liang, C., Song, X., & Huang, J. (2004). Tomographic inversion of Pn travel times in China. *Journal of Geophysical Research Atmospheres*, 109(B11). <https://doi.org/10.1029/2003JB002789>
- Liang, C. T., Huang, Y. L., Wang, C. L., et al. (2018). Progress in the studies of the seismic gap between the 2008 Wenchuan and 2013 Lushan earthquakes. *Chinese Journal of Geophysics (in Chinese)*, 61(5), 19,996–12,010. <https://doi.org/10.6038/Cj2018M0254>
- Lin, F., & Ritzwoller, M. H. (2011a). Helmholtz surface wave tomography for isotropic and azimuthally anisotropic structure. *Geophysical Journal International*, 186(3), 1104–1120. <https://doi.org/10.1111/j.1365-246X.2011.05070.x>
- Lin, F., & Ritzwoller, M. H. (2011b). Apparent anisotropy in inhomogeneous isotropic media. *Geophysical Journal International*, 186(3), 1205–1219. <https://doi.org/10.1111/j.1365-246X.2011.05100.x>

- Lin, F., Ritzwoller, M. H., Snieder, R., et al. (2009). Eikonal tomography: Surface wave tomography by phase front tracking across a regional broad-band seismic array[J]. *Geophysical Journal International*, 177(3), 1091–1110. <https://doi.org/10.1111/j.1365-246X.2009.04105.x>
- Lin, F., Ritzwoller, M. H., Yang, Y., Moschetti, M. P., & Fouch, M. J. (2011). Complex and variable crustal and uppermost mantle seismic anisotropy in the western United States[J]. *Nature Geoscience*, 4(1), 55–61. <https://doi.org/10.1038/ngeo1036>
- Liu, Q. Y., Li, Y., Chen, J. H., et al. (2009). Wenchuan Ms8.0 earthquake: Preliminary study of the S-wave velocity structure of the crust and upper mantle. *Chinese J. Geophys. (in Chinese)*, 52(2), 309–319. [https://doi.org/10.1016/S1874-8651\(10\)60080-4](https://doi.org/10.1016/S1874-8651(10)60080-4)
- Liu, Q. Y., Van Der Hilst, R. D., Li, Y., Yao, H. J., Chen, J. H., Guo, B., et al. (2014). Eastward expansion of the Tibetan Plateau by crustal flow and strain partitioning across faults. *Nature Geoscience*, 7(5), pp. 361–365. <https://doi.org/10.1038/ngeo2130>
- Liu, Y., & Holt, W. E. (2015). Wave gradiometry and its link with Helmholtz equation solutions applied to USArray in the eastern U.S. *Journal of Geophysical Research*, 120(8), 5717–5746. <https://doi.org/10.1002/2015jb011982>
- Liu, Z., Liang, C., Hua, Q., Li, Y., Yang, Y., He, F., & Fang, L. (2018). The seismic potential in the seismic gap between the Wenchuan and Lushan earthquakes revealed by the joint inversion of receiver functions and ambient noise data. *Tectonics*, 37(11), 4226–4238. <https://doi.org/10.1029/2018TC005151>
- Maeda, T., Nishida, K., Takagi, R., & Obara, K. (2016). Reconstruction of a 2D seismic wavefield by seismic gradiometry. *Progress in Earth and Planetary Science*, 3(1), 1–17. <https://doi.org/10.1186/s40645-016-0107-4>
- Matsushita, R., Imanishi, K., Ohtani, M., Kuwahara, Y., Chen, J., & Ma, S. (2019). Seismic potential around the northeastern edge of the Longmenshan fault zone as inferred from seismological observations. *Pure and Applied Geophysics*, 177(1), 37–53. <https://doi.org/10.1007/s00024-019-02098-3>
- Mattatall, L. R., & Fouch, M. J. (2007). Small-scale variations in SKS splitting near Parkfield, California[C]//Agu Fall Meeting. *AGU Fall Meeting Abstracts*. <https://ui.adsabs.harvard.edu/#abs/2007AGUFM.T53C..02M/abstract>
- McNamara D E, Walter W R and Owens T J. 1997. Upper mantle velocity structure beneath Tibet plateau from Pn travel time tomography. *Journal of Geophysical Research*, 102, 493–505. <https://doi.org/10.1029/96jb02112>
- Molnar, P., England, P., & Martinod, J. (1993). Mantle dynamics, uplift of the Tibetan Plateau, and the Indian monsoon. *Reviews of Geophysics*, 31(4), 357. <https://doi.org/10.1029/93rg02030>
- Ni, J. F., Guzman-Speziale, M., Bevis, M., Holt, W. E., Wallace, T. C., & Seager, W. (1989). Accretionary tectonics of Burma and the three-dimensional geometry of the Burma subduction zone. *Geology*, 17, 68–71. [https://doi.org/10.1130/0091-7613\(1989\)017<0068:ATOBAT>2.3.CO;2](https://doi.org/10.1130/0091-7613(1989)017<0068:ATOBAT>2.3.CO;2)
- Nissen-Meyer, T., Fournier, A., & Dahlen, F. A. (2004). The axisymmetric spectral element method for elastic wave propagation[C]//AGU Spring Meeting. *AGU Spring Meeting Abstracts*. <https://ui.adsabs.harvard.edu/#abs/2004AGUSM.S51A..04N/abstract>
- Pandey, S., Yuan, X., Debayle, E., Tilmann, F., Priestley, K., & Li, X. (2015). Depth-variant azimuthal anisotropy in Tibet revealed by surface wave tomography. *Geophysical Research Letters*, 42(11), 4326–4334. <https://doi.org/10.1002/2015gl063921>
- Poppeliers, C. (2010). Seismic wave gradiometry using the wavelet transform: Application to the analysis of complex surface waves recorded at the Glendora Array, Sullivan, Indiana, USA. *Bulletin of the Seismological Society of America*, 100(3), 1211–1224. <https://doi.org/10.1785/0120090304>
- Poppeliers, C. (2011). Multiwavelet seismic-wave gradiometry. *Bulletin of the Seismological Society of America*, 101(5), 2108–2121. <https://doi.org/10.1785/0120100226>
- Poppeliers, C., & Punosevac, P. (2013). Three-dimensional wave gradiometry for polarized seismic waves. *Bulletin of the Seismological Society of America*, 103(4), 2161–2172. <https://doi.org/10.1785/0120120165>
- Poppeliers, C., Punosevac, P., & Bell, T. (2013). Three-dimensional seismic-wave gradiometry for scalar waves. *Bulletin of the Seismological Society of America*, 103(4), 2151–2160. <https://doi.org/10.1785/0120120224>
- Porter, R., Liu, Y., & Holt, W. E. (2016). Lithospheric records of orogeny within the continental U.S. *Geophysical Research Letters*, 43(1), 144–153. <https://doi.org/10.1002/2015GL066950>
- Royden, L. H., Burchfiel, B. C., King, R. W., Wang, E., Chen, Z. L., Shen, F., et al. (1997). Surface deformation and lower crustal flow in eastern Tibet. *Science*, 276(5313), 788–790. <https://doi.org/10.1126/science.276.5313.788>
- Sayers, C. M. (1994). The elastic anisotropy of shales. *Journal of Geophysical Research Solid Earth*, 99(B1), 767–774. <https://doi.org/10.1029/93JB02579>
- Searle, M. P., Windley, B. F., Coward, M. P., et al. (1987). The closing of Tethys and the tectonics of the Himalaya. *Geological Society of America Bulletin*, 98(6), 678–701. [https://doi.org/10.1130/0016-7606\(1987\)98<678:tcot>2.0.co;2](https://doi.org/10.1130/0016-7606(1987)98<678:tcot>2.0.co;2)
- Smith, M. L., & Dahlen, F. A. (1973). The azimuthal dependence of Love and Rayleigh wave propagation in a slightly anisotropic medium[J]. *Journal of Geophysical Research*, 78(17), 3321–3333. <https://doi.org/10.1029/jb078i017p03321>
- Sol, S., Meltzer, A., Bürgmann, R., van der Hilst, R. D., King, R., Chen, Z., et al. (2007). Geodynamics of the southeastern Tibetan Plateau from seismic anisotropy and geodesy. *Geology*, 35(6), 563. <https://doi.org/10.1130/g23408a.1>
- Sollberger, D., Schmelzbach, C., Robertsson, J. O A., et al. (2016). First seismic shear wave velocity profile of the lunar crust as extracted from the Apollo 17 active seismic data by wavefield gradient analysis[C]//EGU General Assembly. https://ui.adsabs.harvard.edu/link_gateway/2016EGUGA18.4020S/PUB_PDF
- Soto, L., Sandvol, E., Ni, J. F., Flesch, L., Hearn, T. M., Tilmann, F., et al. (2012). Significant and vertically coherent seismic anisotropy beneath eastern Tibet[J]. *Journal of Geophysical Research: Solid Earth*, 117. <https://doi.org/10.1029/2011JB008919>
- Stein, S., & Wyssession, M. (2003). Introduction to seismology. *Earthquakes and Earth Structures*. Blackwell Publishing. <https://doi.org/10.1029/2003EO220007>
- Su, W., Wang, C. Y., & Huang, Z. X. (2008). Azimuthal anisotropy of Rayleigh waves beneath the Tibetan Plateau and adjacent areas. *Science in China Series D: Earth Sciences*, 51(12), 1717–1725. <https://doi.org/10.1007/s11430-008-0137-x>
- Sun, C. Q., Lei J. S., Zhu, D. F. (2014). Review of the study on crustal anisotropy by shear wave splitting analysis. *CT Theory and Applications*, 23(4), 687–697. [https://doi.org/10.1004/4140\(2014\)04-0687-11](https://doi.org/10.1004/4140(2014)04-0687-11)
- Sun, X., Bao, X., Xu, M., Eaton, D. W., Song, X., Wang, L., et al. (2015). Crustal structure beneath SE Tibet from joint analysis of receiver functions and Rayleigh wave dispersion. *Geophysical Research Letters*, 41(5), 1479–1484. <https://doi.org/10.1002/2014GL059269>
- Sun, Y., Niu, F., Liu, H., Chen, Y., & Liu, J. (2012). Crustal structure and deformation of the SE Tibetan plateau revealed by receiver function data. *Earth Planet. Sci. Lett.*, 349–350, 186–197. <https://doi.org/10.1016/j.epsl.2012.07.007>
- Tang, Y. C., Tao, K., & Niu, F. L. (2017). Detecting slow velocity anomalies in deep mantle from wave form distortion of teleseismic event. *Chinese J. Geophys. (in Chinese)*, 60(10), 3753–3764. <https://doi.org/10.6038/cjg20171106>
- Tapponnier, P., Peltze, G., Le Dain, A. Y., Armijo, R., & Cobbold, P. (1982). Propagating extrusion tectonics in Asia: New insights from simple experiments with plasticize. *Geology*, 10, 611–616. [https://doi.org/10.1130/0091-7613\(1982\)10<611:petian>2.0.co;2](https://doi.org/10.1130/0091-7613(1982)10<611:petian>2.0.co;2)

- Wang, C., Chang, L., Wei, S., et al. (2008). A model of mechanically coupled deformation in lithosphere beneath the eastern Tibetan Plateau and its vicinity. *Earth Science Frontiers*. <http://search.cnki.net/down/default.aspx?filename=DXQY200806030&dbcode=CJFD&year=2008&dflag=pdfdown>
- Wang, C., Liang, C., Deng, K., et al. (2018). Spatiotemporal distribution of microearthquakes and implications around the seismic gap between the Wenchuan and Lushan earthquake. *Tectonics*, 37(8), 2695–2709. <https://doi.org/10.1029/2018TC005000>
- Wang, C., Lou, H., Silver, P. G., Zhu, L., & Chang, L. (2010). Crustal structure variation along 30°N in the eastern Tibetan Plateau and its tectonic implications. *Earth and Planetary Science Letters*, 289(3), 367–376. <https://doi.org/10.1016/j.epsl.2009.11.026>
- Wang, Z., Fukao, Y., & Pei, S. (2009). Structural control of rupturing of the Mw7. 9 2008 Wenchuan Earthquake, China. *Earth and Planetary Science Letters*, 279(1–2), 131–138. <https://doi.org/10.1016/j.epsl.2008.12.038>
- Wielandt, E. (1993). Propagation and structural interpretation of non-plane waves. *Geophysical Journal International*, 113(1), 45–53. <https://doi.org/10.1111/j.1365-246X.1993.tb02527.x>
- Xie, J., Ritzwoller, M. H., Shen, W., Yang, Y., Zheng, Y., & Zhou, L. (2013). Crustal radial anisotropy across Eastern Tibet and the Western Yangtze Craton. *Journal of Geophysical Research*, 118(8), 4226–4252. <https://doi.org/10.1002/jgrb.50296>
- Xie, J., Ritzwoller, M. H., Shen, W., & Wang, W. (2017). Crustal anisotropy across eastern Tibet and surroundings modeled as a depth-dependent tilted hexagonally symmetric medium. *Geophysical Journal International*, 209(1), 466–491. <https://doi.org/10.1093/gji/ggx004>
- Xu, T., Zhang, Z. J., Liu, B. F., Chen, Y., Zhang, M. H., Tian, X. B., et al. (2015). Crustal velocity structure in the Emeishan large igneous province and evidence of the Permian mantle plume activity. *Science China Earth Sciences*, 58(7), 1133–1147. <https://doi.org/10.1007/s11430-015-5094-6>
- Xu, X., Wen, X., Zheng, R., Ma, W., Song, F., & Yu, G. (2003). Pattern of latest tectonic motion and its dynamics for active blocks in Sichuan-Yunnan region, China. *Science in China Series D: Earth Sciences*, 46(2), 210–226. <https://doi.org/10.1360/03zd20017>
- Xu, Z., Jiang, M., Yang, J. S., Zhao, G. G., Cui, J. W., & Li, H. B. (1999). Mantle diapir and inward intracontinental subduction: A discussion on the mechanism of uplift of the Qinghai-Tibet Plateau. *Special Paper of the Geological Society of America*, 328, 19–31. <https://doi.org/10.1130/0-8137-2328-0.19>
- Yang, Y., Liang, C., Fang, L., et al. (2018). A comprehensive analysis on the stress field and seismic anisotropy in eastern Tibet. *Tectonics*, 37(6), 1648–1657. <https://doi.org/10.1029/2018TC00501>
- Yang, Y., Liang, C., Li, Z., Su, J., Zhou, L., & He, F. (2017). Stress distribution near the seismic gap between Wenchuan and Lushan earthquakes. *Pure and Applied Geophysics*, 174(6), 2257–2267. <https://doi.org/10.1007/s0024-016-1360-6>
- Yao, H., Beghein, C., De Hilst, R. D., et al. (2008). Surface wave array tomography in SE Tibet from ambient seismic noise and two-station analysis—II. Crustal and upper-mantle structure. *Geophysical Journal International*, 173(1), 205–219. <https://doi.org/10.1111/j.1365-246X.2007.03696.x>
- Yao, H., Der Hilst, R. D., & Montagner, J. (2010). Heterogeneity and anisotropy of the lithosphere of SE Tibet from surface wave array tomography. *Journal of Geophysical Research*. <https://doi.org/10.1029/2009JB007142>
- Yu, L. I., Jian, Y. H., Yuan, L. Q., et al. (2010). Phase velocity array tomography of Rayleigh waves in western Sichuan from ambient seismic noise. *Chinese Journal of Geophysics*, 53(4), 842–852. <https://doi.org/10.3969/j.issn.0001-5733.2010.04.009>
- Zhao, B., Huang, Y., Zhang, C., Wang, W., Tan, K., & Du, R. (2015). Crustal deformation on the Chinese mainland during 1998–2014 based on GPS data. *Geodesy and Geodynamics*, 6(1), 7–15. <https://doi.org/10.1016/j.geog.2014.12.006>
- Zhang, Z. (2009). A discussion on some important problems concerning the Emeishan large igneous province. *Geology in China*, 36(3), 634–646. [https://doi.org/10.1016/S1874-8651\(10\)60080-4](https://doi.org/10.1016/S1874-8651(10)60080-4)
- Zheng, T., Ding, Z., Ning, J., Chang, L., Wang, X., Kong, F., et al. (2018). Crustal azimuthal anisotropy beneath the southeastern Tibetan Plateau and its geodynamic implications. *Journal of Geophysical Research Solid Earth*. <https://doi.org/10.1029/2018JB015995>
- Zhou, L., Liang, C., & Yang, Y. H. (2017). Application of three-component seismic-wave gradiometry for the Central and Eastern United States. *Chinese Journal of Geophysics*. <https://doi.org/10.6038/cjg20170907>
- Zhou, S. (2008). Seismicity simulation in Western Sichuan of China based on the fault interactions and its implication on the estimation of the regional earthquake risk. *Chinese Journal of Geophysics*, 51(1), 132–142. <https://doi.org/10.1002/cjg2.1202>
- Zhu, J. S., Wang, X. B., Yang, Y. H., Fan, J., & Cheng, X. Q. (2017). The crustal flow beneath the eastern margin of the Tibetan plateau and its process of dynamics. *Chinese Journal of Geophysics*. <https://doi.org/10.6038/cjg20170602>